






# Hydrogeochemical and geophysical investigations to delineate underground water aquifer in arid regions: A case study, Gara oasis, Egypt

Mohamed NAZIH<sup>1</sup> , Mohamed Mostafa GOBASHY<sup>1,\*</sup> ,  
Zenhom SALEM<sup>2</sup> , Khaled Soliman SOLIMAN<sup>1</sup> ,  
Ahmed AbdelHalim M. HASSAN<sup>3</sup> 

<sup>1</sup> Cairo University, Faculty of Science, Geophysics department, Giza, Egypt;  
e-mails: mohamednazih736@yahoo.com, gobashy@sci.cu.edu.eg,  
khaled\_soliman2005@yahoo.com

<sup>2</sup> Tanta University, Faculty of Science, Geology department, Tanta, Egypt;  
e-mail: zenhomsalem@yahoo.com

<sup>3</sup> Cairo University, Faculty of Science, Geology department, Giza, Egypt;  
e-mail: ahmedabdelhalim@cu.edu.eg

**Abstract:** The goal of the present study is to investigate, delineate, and evaluate the shallow Miocene groundwater aquifer with vertical and lateral facies variations in the Gara oasis, western desert of Egypt. This oasis represents a typical arid region in North Africa. Through grid texture analysis, lineament detection, edge detection, thresholding, and identifying areas of structural complexity from the filtered residual reduced-to-pole magnetic anomaly map, it is possible to outline the fracture zones that principally control the groundwater aquifers and water flow in the area. The groundwater quality and quantity are examined hydro-geochemically through nine groundwater samples that were gathered from wells and springs distributed throughout the area around Gara Lake. Measurements of physio-chemical parameters (TDS, pH, and EC) are carried out and its spatial distribution is critically studied. The results reveal that the ion-exchange process caused by water-rock interaction is the dominant process. Furthermore, the main ions in the groundwater in the study areas were Na and Cl. This might be due to evaporation or halite dissolution with the upward flow of waters through the fractures from the deep aquifer of the Nubian sandstone to the shallow aquifer of the fractured Miocene limestone.

**Key words:** arid regions, Gara oasis, hydrogeochemistry, magnetic, grid analysis, Western desert, groundwater aquifer

---

\*corresponding author, e-mail: gobashy@sci.cu.edu.eg

## 1. Introduction

Groundwater has been a major challenge to sustainable agricultural expansion in the oasis of Egypt's northwestern desert (NWD) during the last few decades in accordance with the needs of agricultural, tourist, and economical evolution (*Al-Omran et al., 2013; Aly et al., 2011*). Several wells were developed in response to the increased agricultural land, urbanization developments, and food industries (*Salheen, 2013*). The inadequate dispersion of all these wells and excessive groundwater began to reduce both the pressure head and the groundwater quality (*Dahab, 2004*). This is a prevalent problem in Siwa (SO) and Gara oasis (GO), both in Egypt's NWD. Unfortunately, especially in GO, drilling for water supply continues to occur without permission, requiring further hydrogeochemical investigations to detect changes in the quantity and quality of groundwater resources. An extensive assessment of groundwater potential may be performed by evaluating recharge sources, whether they are from surficial water infiltration or migrating, as well as significant structural and fault systems from surrounding aquifers. The Gara depression, located in Egypt's north-western corner (Fig. 1), and the closest depression to SO, is considered as one of the desert areas that have no running canals or streams, furthermore, it is distinguished by a common hot climate that is described by the poverty of rains, high temperature, consequently over evaporation. Therefore, in all different fields, GO is essentially a typical arid region dependent on groundwater, in particular, brackish water that flows from the limestone fractured Miocene aquifer (shallow), distinguished as the source for farming of agricultural, manufacturing, and constructive improvement in the region (*El Hossary, 2013; Abo El-Fadl et al., 2015; Aly, 2015; Gad et al., 2018; Aly, 2020*). In the Gara and Siwa depressions, artesian wells from the upper shallow Miocene groundwater aquifer represent an established and conventional source of irrigation water (*Aly et al., 2016*). Due to the explicit requirement for more undeveloped land, the upper shallow Miocene limestone aquifer has been explored by excavating and borehole drilling to reveal significant sources of irrigation water (*Aly, 2001*). The total number of artesian wells has exceeded 900. Because of the oasis's continuous agricultural development and expanding demand for water resources, as evidenced by increased water consideration, there is a critical need for evaluating water quantity

and quality in the Gara and Siwa depressions (*Aly and Benaabidate, 2010; Aly et al., 2016*). The magnetic method, on the other hand, is a geophysical method that can be utilized in hydrogeological investigations. The magnetic technique is the most flexible of all geophysical techniques since it may be employed in both shallow and deep studies (*Dobrin and Savit, 1988*). It is also inexpensive including both regional and local investigations. The magnetic method has mostly been used for regional surveys in hydrocarbon exploration (*Abdelazeem et al., 2020, 2021; de Smet et al., 2021; Abdelrahman et al., 2019; Kwami et al., 2018; Abdulrahman et al., 2017; Helaly, 2017; Gobashy and Al-Garni, 2008; Al-Garni et al., 2006*); engineering geophysics (*Araffa et al., 2021; Abdelazeem et al., 2014*); groundwater exploration (*Gobashy et al., 2021b; Al-Garni et al., 2006*); mineral exploration (*Gobashy et al., 2020, 2021a; El-Sawy et al., 2018; Abdelrahman et al., 2019*), mapping geological structures and igneous intrusions (*Al-Garni et al., 2012; Ndatuwong and Yadav, 2014; Wang et al., 2017; El-Sawy et al., 2018*); archaeo-geophysics (*Schneidhofer et al., 2017*); as well as estimating sedimentary basin thickness and identify groundwater contamination (*Rehman et al., 2019*) and geologic hazard and risk assessments (*Fergany et al., 2015; Al-Garni and Gobashy, 2010*) are examples of such wide range of applications.

The main targets of this work are to delineate the subsurface structures in the GO area, and their effects on the groundwater including the characteristics of the aquifer, and their hydrochemical properties. The aeromagnetic RTP map was used for obtaining the regional subsurface structures that may control the groundwater aquifer. The study provides also a detailed hydrogeochemical study on the shallow aquifer groundwater in the GO area.

## 2. Geology

Gara oasis (GO) is located on the western limb of Egypt's Qattara Depression, which extends from west to east (Fig. 1). A critical part of the GO depression is beneath sea level; at its deepest about 60 m, making it Egypt's second-lowest point after Qattara (133 m beneath sea level). It is bordered by steep slopes on both the northern and southern sides, and the west side is graded into upper Eocene to lower Miocene clastic. The depression is con-

sidered to have developed as a result of the interaction of salt weathering and wind erosion (*Said, 1990; Ayyad and Ismail, 1992; Orabi et al., 2015; Osman and Orabi, 2017* and others). The salt crumbles the depression floor due to the severe Aeolian weathering, and the resultant sands are carried away by the wind (*Elzarka and Radwan, 1986; El-Khoriby, 1994*).

To understand the geochemical footprint of different water aquifers in the GO the surface and subsurface hydrogeological units were introduced and described.

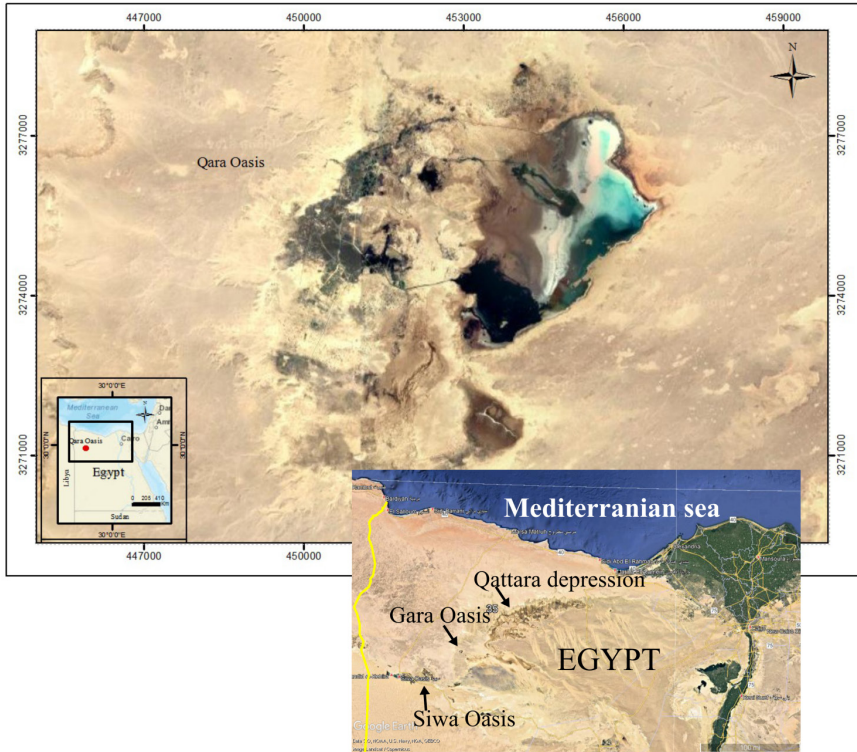


Fig. 1. Satellite image of Gara area.

## 2.1. Geological settings

The Gara depression developed as a dome formation that was fragmented by karstic processes during the late Miocene period and then developed by

deflation and substantially altered by mass wasting and fluvial processes (Elzarka and Radwan, 1986; Said, 1990; Orabi et al., 2015). The depression is dug in Tertiary sedimentary strata ranging from the Middle Eocene Mokattam group to the Middle Miocene Marmarika formation (Fig. 2). On the NE side, there is a regional dip of a few degrees toward the N–NW.

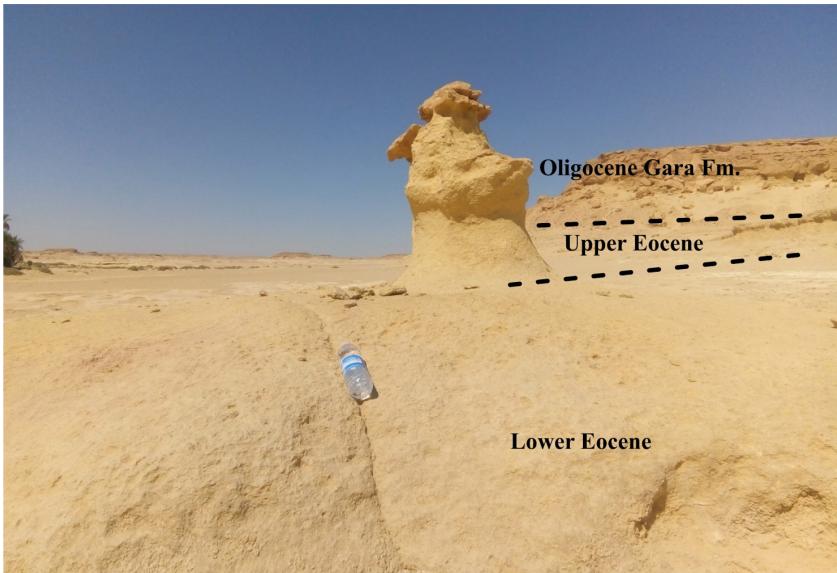


Fig. 2. The stratigraphic succession of Gara floor.

As part of the El Diffa plateau, the steep northern wall is the scarp slope of a cuesta covered by middle Miocene carbonate rocks (Orabi et al., 2015). Its gently sloped edges decline to sediments inclined southerly, leading to hidden rivers and sinkholes with no established downstream location. A certain section downstream, which is now extensively coated with saline crusts, sabkha deposits, and salt marshes, declines southward into the basin's deeper quadrangular portion, where it has been estimated that there are elevations as deep as 18 meters below sea level. Sinkholes and cavernous sub-surface limestone in the area indicate to karstic development in the past (Raid, 2001). Furthermore, karstification occurred during the late Miocene, wherever the Mediterranean Sea returned while north-dipping aquifers were discharged, leaving an empty basin (Moussa, 2006; El Gammal, 2010).

As the Mediterranean Sea receded, what is now the Western Desert of Egypt and its off-shore continuations were subjected to extensive erosion by streams. A significant stream originating in the Gilf-Kebir Mountainous region migrated northward to near the current locations of Siwa and Gara depression, then through Libya's Sahabi Channel System, or via a much shorter path through the Qattara zone to a discharge near the edges of the Ras Alam El Rum submarine valley away from the shore near Alexandria. During these circumstances, the Qattara depression is produced by a stream that is either a branch of the Gilf River or a portion of that river's descending path into the Mediterranean Basin (*Abdel-Rahman et al., 1980; Said, 1990; Hammad et al., 2000*), Its waters were supposedly redirected into underground streams via drains and caves, rendering it inactive (Figs. 3 and 4).



Fig. 3. Karst escarpment observed in GO.

The produced geological map dominated the main rock units exposed on the surface of the GO which can be differentiated into (Fig. 5):

- Mokattam group (Middle Eocene to Upper Eocene),
- Gara Fm (Oligocene),
- Moghra Fm (Middle Miocene),
- Marmarica Fm (Middle Miocene to upper Miocene),
- Sabkha (Karshef).



Fig. 4. Karst caves in limestone succession at GO.

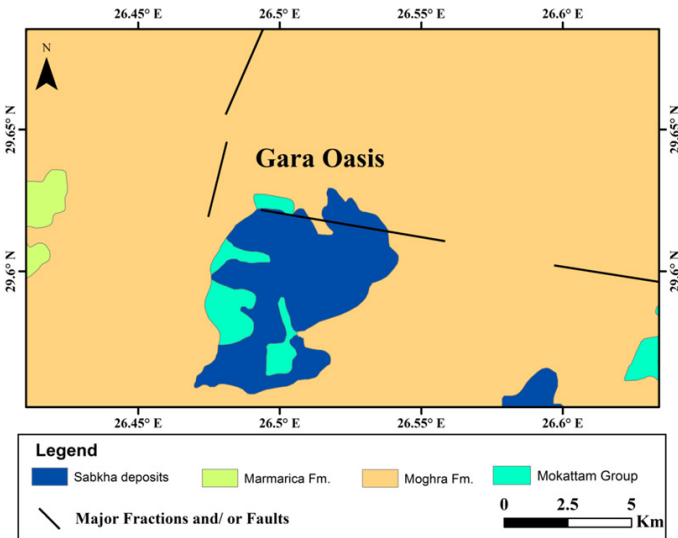


Fig. 5. Simplified geological map of Gara depression.

**Mokattam group:**

These rock units could be divided in the study area into two main units the lower with chalky and hard limestone with fractures and some caves called Mokattam Formation. On the other hand, the second unit is characterized by enrichment of fossils (Nummelites) which are characterized by yellowish-white in color with marly limestone interbeds and extensive fractures and caves of different sizes and geometry that called the Hamra Formation (Figs. 4 and 6).



Fig. 6. Fractured limestone of Mokattam Group (Middle-Upper Eocene).

**Gara Formation:**

The Eocene succession was followed by cross-bedded limestone with intercalation of shale and silt that named the Gara Formation according to *Orabi et al. (2015)*, and *Osman and Orabi (2017)*. This rock unit is equivalent to Hamra member of Naqb Ahmer southwest of GO, which dominated with variegated shale and silt, and iron-manganese concretions which changed northward with cross-bedded limestone (Fig. 7).





Fig. 7. Cross bedded and reworked limestone with clastics intercalation and concretions.

### **Moghra Formation:**

In the south to southeast of the GO, Moghra Middle Miocene lithologic units are widely exposed, consisting primarily of interbedded fossiliferous shale, sandstone, gypsiferous claystone, and limestone, with the top part consisting of continental to a shallow marine siliciclastic distribution including siltstone, shale, and white sandy carbonate beds, with sufficient shell fragments (Fig. 8).

### **Marmarica Formation:**

Marmarica is mainly composed of greyish white calcarenites with minor shale interactions, followed by white limestone rich in fossils in the Miocene (Fig. 9).

### **Sabkha (Karshef):**

Sabkha sediments composed of salt mixed with Quaternary deposits of silt, sand, and clay intercalated with evaporates, which is locally named Karshef (Fig. 10).



Fig. 8. Moghra shale recorded outside the Gara depression to the southeast and northeast.



Fig. 9. Maramarica formation as a part of El Diffa plateau.

## 2.2. Subsurface geology of Gara

### Near Gara wells:

Because the GO has an insufficiency of drilled wells, the description of the subsurface of the GO has been dependent on the two nearby wells of Gibb Afia-1 and Gibb Afia-2 wells (Figs. 11 and 12).



Fig. 10. Karshef deposits (salty clastics).

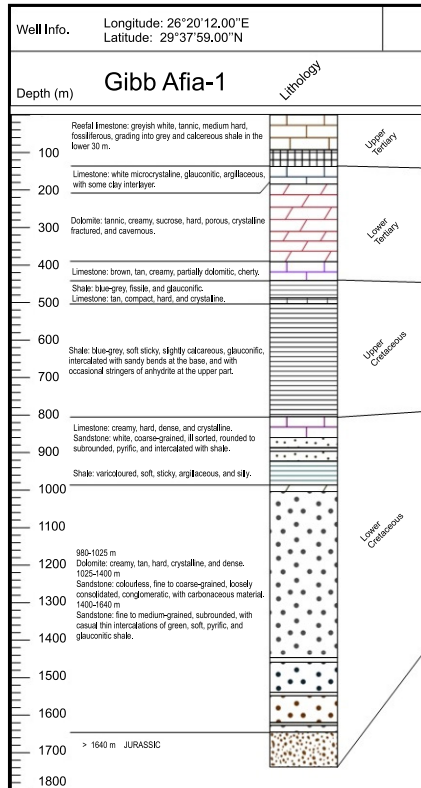


Fig. 11. Litho stratigraphic section of Gibb Afia-1 well (modified after GPC, 1973).

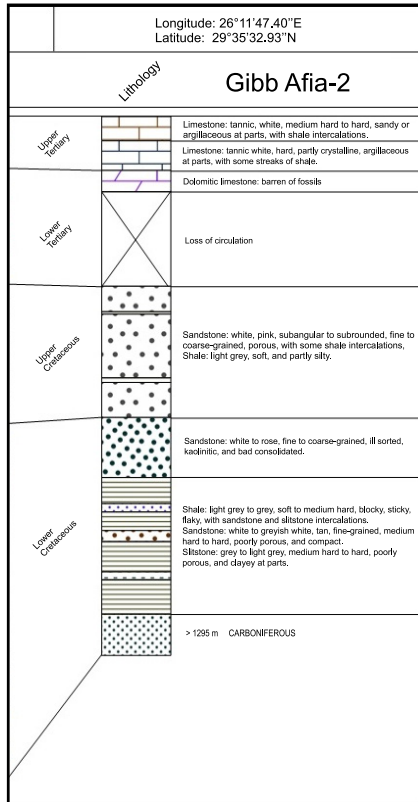


Fig. 12. Litho stratigraphic section of Gibb Afia-2 well (modified after *GPC, 1973*).

**Gibb Afia-1 well**

To the west of the Qattara Depression is the Gibb Afia area. It is categorized as an anticlinal structure because of its prominent positive gravity and surface geology. In the years 1955 to 1956, the Sahara Petroleum Company (Sapetco) conducted a regional gravity survey that covered an extended area of the Western Desert including the Gibb Afia concession. The Gibb Afia structure appears on the constructed map as a positive feature, within the Bouguer anomaly counter of 10.0 mgl. The Gibb Afia structure lies at the West-South-West part of the Qattara Depression. The Gibb Afia-1 well was drilled in 1956 on the far eastern part of this seismic structure. However, the well was located away from the gravity maximum by about 13 km.

In Gibb Afia-1 well gas shows were recorded in 3 horizons; Lower Eocene, Lower Cretaceous, and Paleozoic (Fig. 11). These gas shows are worth to be mentioned because the Gibb Afia structure could be considered a perfect trap for oil/gas. The complication of available geophysical and geological data revealed that the Gibb Afia-1 well lies off the mentioned structure. Hence, those recorded gas shows would be a good prospective target in a better structural position.

### **Stratigraphic analysis**

The penetrated stratigraphic section in Gibb Afia-1 well will be described in the following, from top to bottom, and the lithostratigraphic succession of the studied interval (Fig. 11).

#### **Tertiary** (Depth 0 – 420 m, thickness 420 m)

The Tertiary sequence in the Gibb Afia-1 well comprises 180 m thick Miocene and 240 m thick Eocene sedimentary rocks. It overlies unconformably the Cretaceous deposits (at drill depth 240 m).

#### **Miocene**

##### **Middle Miocene** (0 to 130 m in depth, and 130 m in thickness)

The reddish to grey-white, medium-hard, extremely fossiliferous limestone of the Middle Miocene gives way to green to grey, calcareous shale in the lower 30 meters. The faunal composition identified in this study suggests offshore marine deposition in Refael environments. The Gibb Afia-1 well's Middle Miocene interval is part of the Marmarica Formation.

##### **Lower Miocene** (130 to 180 m in depth, and 50 m in thickness)

The Lower Miocene section in Gibb Afia-1 well consists of limestone, white to creamy, microcrystalline, highly glauconitic, argillaceous, with some clay interlayers. The entire section belongs to the Mamura Formation. The Lower Miocene section is unconformably overlying the Middle Eocene deposits. The Oligocene and Upper Eocene deposits are absent in Gibb Afia-1 well.

#### **Eocene**

##### **Middle Eocene** (180 to 375 m in depth, and 195 m in thickness)

Within this interval, the drilling of the Gibb Afia-1 well was accompanied by loss of circulation. Thus, the lithological description can be only estimated

approximately. The Middle Eocene section consists of dolomite, which is tan to cream, sucrose, hard, porous, crystalline, fractured, and cavernous. This dolomitic section probably belongs to the Apollonia Formation.

**Lower Eocene** (375 to 420 m in depth, and 45 m in thickness)

The Lower Eocene section in Gibb Afia-1 well consists mainly of limestone. It is brown to cream, partially dolomitic, cherty, and grading into grey, partially conglomeratic shale. This limestone belongs to the Apollonia Formation. The Lower Eocene section is unconformably overlying the Turonian deposits. The Palaeocene and uppermost Upper Cretaceous deposits are absent in Gibb Afia-1 well.

**Cretaceous** (420 to 1640 m in depth, and 1220 m in thickness)

The Cretaceous succession is subdivided into the Upper Cretaceous section (420–800 m), and Lower Cretaceous section (800–1640 m).

**Upper Cretaceous**

**Turonian** (420 to 500 m in depth, and 80 m in thickness)

The Turonian section in Gibb Afia-1 well consists mainly of shale and limestone. The shale is blue to grey, fissile, and glauconitic. The limestone is tan, compact, hard, and crystalline. It belongs to Abu Roash Formation.

**Cenomanian** (500 to 800 m in depth, and 300 m in thickness)

The Cenomanian deposits in the Gibb Afia-1 well are of a typical marine environment and contain fossiliferous shale. It is grey to blue, soft sticky, slightly calcareous, highly glauconitic, and intercalated with sandy bands at the base and with occasional stringers of anhydrite at the upper part of the section. The entire Upper Cretaceous section in Gibb Afia-1 well belongs to the Bahariya Formation.

**Lower Cretaceous**

**Albian** (800 to 980 m in depth, and 180 m in thickness)

The upper part of the Albian section in the Gibb Afia-1 well consists of thick carbonate deposits. The limestone is creamy, hard, dense, and crystalline. The limestone is followed by coarse-grained sandstone, ill sorted, rounded to subrounded, pyritic, and intercalated with shale streaks and bands. The lower part of the Albian section consists of varicoloured shale. It is pink,

blue, grey-red, soft, sticky, argillaceous, and silty. The entire Albian section belongs to the Kiiarita Member of Burg El Arab Formation.

### **Aptian** (980 to 1640 m in depth, and 660 m in thickness)

According to the previous work done by the Sahara Petroleum Company (Sapetco), this part of the section was regarded to be of "undifferentiated Lower Cretaceous" with the single faunal species *Chojfatella* sp., which was found in a core sample at drill depth 1021 m, and was considered later as of Aptian age (*Kazatchenko et al., 1970*). The upper part of the Aptian section in the Gibb Afia-1 well (980–1025 m) is characterised by the abundance of dolomite and carbonate deposits. The dolomite is cream-colored, hard, crystalline, and dense, with a very high resistivity on the electric logs. It should be considered as an equivalent to the Aptian dolomite, especially since it was accompanied by a good gas kick during its penetration. The interval from 1025 to 1400 m consists of sandstone and shale intercalations. The sandstone is colourless, fine to coarse-grained, conglomeratic, with carbonaceous material. The shale is varicoloured, soft, glauconitic, and carbonaceous. The lower part of the Aptian section in Gibb Afia-1 well (1400–1640 m) consists of fine to medium-grained, and subrounded sandstone, with thin intercalations of green, soft, pyritic, and glauconitic shale. The entire Aptian section in Gibb Afia-1 well belongs to the Dahab Member of Burg El Arab Formation.

The Aptian section overlies unconformably the Jurassic deposits. The lowermost part of the Lower Cretaceous is absent in Gibb Afia-1 well.

### **Gibb Afia-2 well**

Gibb Afia-2 was the sixth drilling test well of the GPC in the Siwa area. Gibb Afia lies to the west of Qattara Depression. As an anticlinal structure, the area is distinguished by a prominent positive gravity and surface geology. The Sahara Petroleum Company (Sapetco) drilled the Gibb Afia-1 well in 1955 and 1956, which revealed a local Paleozoic uplift. Later (1969–1970) reinterpretation of this data by the GPC proved the misinterpretation of Sapetco for the Gibb Afia structure. The structure's peak was found to be 13 km west of the Gibb Afia-1 well, according to recent seismic results. Faults separate the structure into various blocks, making it more difficult to interpret. In the seismic map, the structure measures 30 × 17 km. Its axis

undulates from the latitudinal trend in the west to the NE at the eastern part.

The available seismic data suggested the presence of the tectonic features dissecting the apical part of the structure longitudinally into blocks. However, the latest seismic interpretation showed the Gibb Afia structure, on the top Palaeozoic, as an anticlinal feature, trending NE–SW, approximately 50 km long and 15 km wide. A fault cutting along its north-western flank and downthrown crosses this anticline to the northwest. The Gibb Afia-2 well reached an area of Upper Cretaceous rock that had been extensively eroded (Fig. 12). The well was a serious complete loss and a fishing job at 2191 m after which it was plugged back and sidetracked at the depth of 1705 m. Most of the sedimentary section penetrated was found to be flooded with fresh water. No oil shows were recorded in the well, and it was plugged back and the area was deserted.

### **Stratigraphic analysis**

The penetrated stratigraphic section in Gibb Afia-2 well will be described in the following, from top to bottom, and the lithostratigraphic succession of the studied interval (Fig. 12).

#### **Tertiary** (0 to 423 m in depth, and 423 m in thickness)

The Tertiary sequence in the Gibb Afia-2 well comprises 82 m thick Middle Miocene, 66 m thick Lower Miocene, and 26 m thick Middle Eocene sedimentary rocks. It overlies unconformably the Cretaceous deposits.

### **Miocene**

#### **Middle Miocene** (0 to 82 m in depth, and 82 m in thickness)

The limestone dominates the upper 30 meters of the Middle Miocene section. It is described as a tannic white to creamy in colour, medium-hard to hard in texture, vuggy, and partially fossiliferous contents. The limestone is followed by a 20-meter layer of sticky tannic grey to greyish-white shale.

The part of the Lower Middle Miocene section is made up of intercalations of limestone and shale. Tannic white to pinkish-white limestone that is medium-hard to hard, sandy, and/or argillaceous in certain parts. The Marmarica Formation covers the whole Middle Miocene portion of Gibb Afia-2 well.



**Lower Miocene** (82 to 148 m in depth, and 66 m in thickness)

The Lower Miocene portion of the Gibb Afia-2 well is mostly limestone with some shale streaks. It is a Tannic white to pinkish-white limestone that is hard, partially crystalline, and argillaceous in parts. The shale is beige with tannic grey, soft to moderately hard, and insignificantly calcareous. The recorded foraminiferal assemblage in this interval reflects a shallow marine depositional environment varying from reefal to lagoonal. The entire section belongs to the Mamura Formation.

**Eocene****Middle Eocene** (148 to 174 m in depth, and 26 m in thickness)

Dolomitic limestone represents the Middle Eocene section in the Gibb Afia-2 well. It is tan, hard, crystalline, light, and compact. This dolomitic limestone is barren of fossils. It is considered an Eocene age based on lithological characteristics. The dolomitic limestone probably belongs to the Apollonia Formation.

In the interval from drill depth 174 to 423 m, the circulation was lost with no recovery. However, there are neither electrical logs nor ditch samples for this interval. It could be interpreted only by the aid of electrical of the water well within the interval 174 to 334 m. This interval is composed of limestone and streaks of shale.

**Cretaceous** (423 to 1295 m in depth, and 872 m in thickness)

The Cretaceous sequence in Gibb Afia-2 well is subdivided into a Cenomanian section (423–782 m), Albian section (782–952 m), and Aptian section (drill depth 952–1295 m).

**Upper Cretaceous****Cenomanian** (423 to 782 m in depth, and 359 m in thickness)

The Cenomanian deposits are mostly sandstone with a few shale intercalations. White, pink, fine to coarse-grained, subangular to subrounded, and porous sandstone. The shale is light grey, soft, and silty in sections. The Bahariya Formation is represented by this clastic section in the Gibb Afia-2 well.

**Albian** (782 to 952 m in depth, and 170 m in thickness)

The clastic section underlying the Cenomanian sediments is devoid of fossils. It is mainly composed of sandstone that is white to rose, fine to coarse-grained, ill sorted, poorly porous, and kaolinitic. This sandstone is considered to be of the Albian age. Therefore, it seems that this 170 m thick clastic section in Gibb Afia-2 well belongs to the Kharita Member of Burg El Arab Formation.

**Aptian** (952 to 1295 m in depth, and 343 m in thickness)

The Aptian portion of the Gibb Afia-2 well is mostly shale intercalated with sandstone and silt. The shale is light grey to grey in colour, soft to medium in hardness, blocky, sticky, and flaky. The sandstone is white to greyish white in colour, tan in texture, fine-grained, medium-hard to hard in hardness, weakly permeable, and compact. The siltstone is grey to light grey in colour, medium-hard to hard in hardness, weakly porous, and micaceous in places. The whole Aptian section of the Gibb Afia-2 well is part of the Burg El Arab Formation's Dahab Member. The underlying sediments date back to the Carboniferous period. The lower Cretaceous, Jurassic, Triassic, and upper Palaeozoic are all absent from the Gibb Afia-2 well.

**The hydrogeological setting (water bearing formation)**

In the GO different water-bearing formations represent the source for groundwater. These are the formations (the shallower aquifer of the Miocene fractured limestone, the intermediate aquifer of the Eocene fractured limestone, and the deeper aquifer of the Cretaceous Nubian sandstone).

Both the Miocene and Eocene water-bearing formations describe the tertiary carbonate aquifer system (TCAS) (*El Hossary, 2013*). The aquifer system of the Nubian Sandstone (NSSAS) is overlaid by the tertiary carbonate aquifer system. The fractured carbonate sections are separated by the low permeability shale and clay layer from the underlying Nubian sandstone. This layer is behaving as a cap rock (*El Hossary, 2013*). The main source of recharge for the aquifers is the upward flow from the NSSAS (*Ibrahim, 1991; Dahab, 2004*). The target zone for our study is the Miocene Carbonate aquifer (Shallow aquifer). The Miocene fractured limestone involves the floor of the depression below the surface part. The wells with depths less than 150 m exhibit a zone of 80 m thick, consisting of hard limestone interbedded with shale has a yield of 960 m<sup>3</sup>/day (*El Hossary, 1999*). The productivity of this aquifer varies from one place to another due to the

variety of fracture occurrences and the extent of its relationship with the source of recharge (Nubian Sandstone aquifer). The various deep drillings of RIGW (1996–1999) exhibit several zones of fractures inside the carbonate aquifers.

### 3. Methodology

#### 3.1. Aeromagnetic data collection and preparation

The aeromagnetic data in this study is extracted from the detailed survey conducted by *EGPC (1989)*; the purpose of this data analysis is to define the regional basic structure of the area in and around the Gara region, as well as to investigate the structural controlling parameters of the depression's shallow and deep groundwater aquifers. This survey data is re-digitized and processed to 674 data points and a reduced-to-pole map is created (Fig. 13a). In order to evaluate the general structure of the Gara region, this map is subjected to several spatial filtering techniques. The FFT2 Transform image of the RTP data's radially averaged power spectrum is calculated (Fig. 13b) and the residual component between the two wavelengths 20200 m and 7750 m is used as a suitable choice based on the geologic structures in the study area. This residual component (Fig. 14) is utilized for further analysis as the target is the shallow part of the earth's crust. The general trends that can be extracted from the residual map are NW–SE, EW, and NE–SW. The NW–SE Cambrian trend matches with the Erythrean faults and the Gulf of Suez trend. This is an old trend that has been rejuvenated periodically mainly during Hercynian, and Alpine Orogenies. The residual component is then subjected to several grid analysis techniques, such as texture analysis, lineament detection, edge detection, thresholding, and structural complexity, using the CET tool of the OASIS montaj<sup>©</sup> software (*Geosoft, 2015*). The result is the identification of common discontinuities in magnetic data.

**Texture analysis:** Texture analysis uses the standard filter (STD) that signifies the dispersion of pixel intensities in the greyscale. This results in high standard variation values in places of discontinuity. Moreover, it defines the regions of complicated textures connected to abrupt changes in magnetic values. Numerically, for a window of  $N$  cells, whose character value is  $\mu$ , the STD ( $\sigma$ ) of the cell values  $X_i$  is provided by:

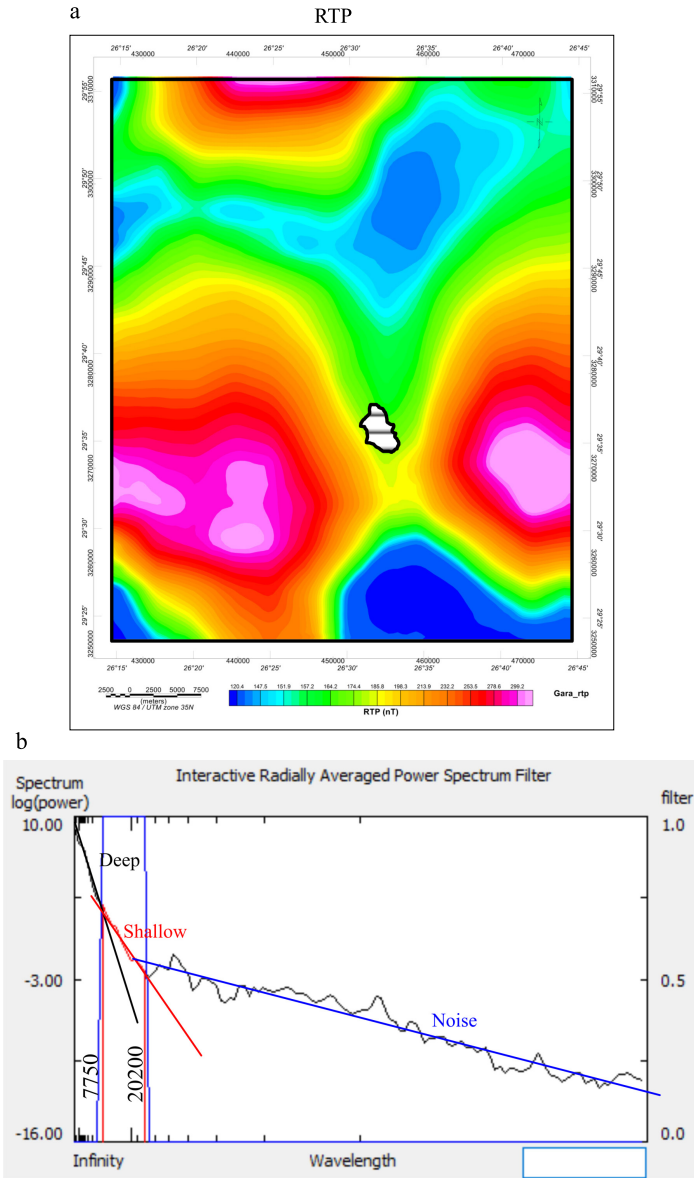


Fig. 13. Magnetic anomaly map (a) of the Gara area reduced to pole (RTP); the corresponding radially averaged power spectrum (b).

$$\sigma = \sqrt{\left[ \frac{1}{N} \sum (X_i - \mu) \right]}. \quad (1)$$

Alternatively, an entropy filter was also shown to improve magnetic anomalies in the area (Holden *et al.*, 2008), by measuring the textural information within the study area. The statistical randomness of neighbourhood data values is measured by quantizing the data into discrete bins and then analysing the total number of distinct values resultants from that quantization. The Entropy map evaluates the complexity and presents the results in an image. The high value of image Entropy implies that the neighbouring pixels have a strong contrast. The image's complex textures are reflected in the image's high entropy (Mohanaiah *et al.*, 2013).

**Lineament detection:** to enhance linear features, two tools for lineation detection area used; Phase Symmetry (PS) which improves the appearance of linear features by highlighting zones that are expected to contain axes of symmetry; and Phase Congruency (PC) which address the discontinuities (or edges) by locating possible edge features by identifying points where local spatial frequencies are in phase.

**Edge detection:** this generates skeletal estimates of features through Amplitude thresholding which applies non-maximal suppression and amplitude thresholding; Skeletonization which decreases feature regions to thin lines; and Skeleton to Vectors which exports the skeletal thin lines to vectors.

**Thresholding and structural complexity:** these are performed by analysing the trend detection output to identify regions of structural complexity.

### 3.2. Analyses and collection of groundwater samples

In September 2019, nine groundwater samples were collected from wells and springs located around the Gara Lake region. In Fig. 19 depicts the locations of the samples, and the hydrogeochemical properties. Physiochemical parameters (TDS, pH, and EC) were measured in the field in actual environments using portable instruments. The pH was obtained using a pH meter–CG 817, TDS were determined in dS/m at 25 °C using an electrical conductivity meter (Test kit Model 1500 20 Cole and Parmer). According to Klute (1986), Ca and Mg were measured utilizing the Versenate titration

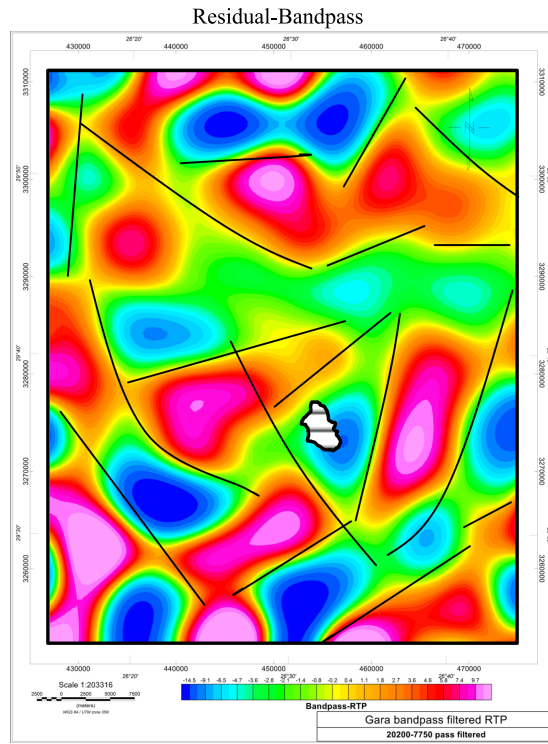


Fig. 14. Residual bandpass filtered anomaly map, Gara area. Possible linear trends are posted as solid lines.

technique (EDTA), A flame photometer was used to estimate Na and K, The chemical titration technique was used to produce Cl and  $\text{HCO}_3$ , and a turbid metric technique spectrophotometer was used to detect  $\text{SO}_4$ . To prevent the effects of stagnant water, water was circulated for around 10 minutes before measurements were collected. One litre of water was collected in two fresh and cleaned plastic bottles for each sample. To overcome metal adsorption to bottle walls and decrease biological activity, water in one bottle was acidified with  $\text{HNO}_3$  to a pH lower than two. At Egypt’s Desert Research Centre, Central Laboratory, water, and soil analysis section, the samples were chemically analysed for major elements using conventional procedures. Total hardness and calcium hardness tests were used to detect the presence of Ca and Mg cations. Following Table 1 summarizes

the analytical parameters of the investigated samples.

Table 1. Results of chemical analyses of the collected water samples.

Well No.					Cations (mg/l)				Anions (mg/l)			CB
	PH	EC ( $\mu\text{s}/\text{cm}$ )	TDS (mg/l)	TH (mg/l)	Ca	Mg	Na	K	HCO <sub>3</sub>	SO <sub>4</sub>	Cl	
GS3	7.9	6480	3598	817.244	156	103.7	1060	46	244	360	1750	1.76
GS5	7.5	10130	6139	1586.788	330	184.9	1550	47	256.2	1273.5	2625	-2.53
GS6	7.4	9840	5134	1403.016	302.8	156.8	1350	45	274.5	391.8	2750	-1.77
GS7	7.3	10220	5897	1566.024	341.8	172.7	1650	45	274.5	600	2950	1.5
GS8	7.5	10910	6102	1648.488	420.6	144.9	1700	44	256.2	614.4	3050	1.88
GS9	7.5	9840	5975	1081.666	332.6	60.7	1850	41	280.6	850	2700	1.83
GS10	7.6	9920	6230	1813.709	390.4	203.3	1300	473	280.6	1073	2650	1.17
GS11	7.6	10340	5778	1893.459	398.4	217.8	1450	42	280.6	629.9	2900	0.79
GS12	7.8	6430	3883	1046.619	139.4	169.4	1040	43	183	599.4	1800	0.36
Min	<b>7.3</b>	<b>6430</b>	<b>3598</b>	<b>817.244</b>	<b>139.4</b>	<b>60.7</b>	<b>1040</b>	<b>41</b>	<b>183</b>	<b>360</b>	<b>1750</b>	<b>-2.53</b>
Max	<b>7.9</b>	<b>10910</b>	<b>6230</b>	<b>1893.459</b>	<b>420.6</b>	<b>217.8</b>	<b>1850</b>	<b>473</b>	<b>280.6</b>	<b>1273.5</b>	<b>3050</b>	<b>1.88</b>
Avg	<b>7.5727</b>	<b>9222.72</b>	<b>5324</b>	<b>1415.247</b>	<b>306.5455</b>	<b>153.8818</b>	<b>1440</b>	<b>121.8182</b>	<b>253.9818</b>	<b>729.5909</b>	<b>2543.182</b>	<b>0.3945</b>
	Chemical balance: CB											

### 3.3. Data representation (spatial and graphical)

The spatial configurations of the parameters are represented as maps. By displaying the concentrations of major ions in the Piper trilinear diagram, the hydrogeochemical facies of groundwater and drifts of salinity progression could be determined (*Chidambaram et al., 2011; Gimenez Forcada, 2010*) and Geochemistry Software AqQA, version AQC10664, utilized to evaluate Schoeller diagrams (*RockWare AqQA software, 2011*). Binary diagrams including Sulin, ionic relationships, Gibbs diagrams were created using Excel program version 2010 Hierarchical cluster analysis (HCA), and Var-Covariance matrix based on Euclidian correlation coefficient were determined utilizing PAST 4.03 (*Hammer et al., 2001*).

## 4. Results

### 4.1. Magnetic analysis

The structural configuration of the study area and the geometrical structure of the shallow and deep aquifers were delineated by grid analysis of the residual signal of the RTP aeromagnetic field of Gara.

A map showing the investigated area's RTP magnetic anomalies (Fig. 13a), Exhibits a magnetic relief of about 60 nT. Three major high magnetic anomalies can be distinguished; the first is toward the west of Gara Lake (A), the second toward the east (B), and the third anomaly toward the north (C). As shown on the Residual bandpass filtered anomaly map, these three anomalies are segregated from the surrounding low magnetic background by possible magnetic contacts or faults (Fig. 14). Considering Fig. 14 indicates that the area is influenced by regional trends including such NE–SW and E–W.

Results of this Grid analysis on the bandpass filtered RTP map of the investigated area using standard deviation (STD) and entropy analysis (EA) are shown in (Fig. 15a). Possible zones of discontinuities are characterized by high STD values, while a Sharp peak with small STD values may indicate a trend caused by fracturing. A broad peak with a large STD may be formed by successive renewals of shifting stress direction.

The STD result was then used to generate the phase symmetry (PS) map (Fig. 15b), which identifies the possible regions of interest and laterally separates the continuous lines (linear structures). The size and orientation of the identified features are determined by the scale and orientation parameters. The PS employs the texture improvement from the STD consequences for identifying zones of lateral discontinuity (Fig. 15b). The effects of PS are used to transform discontinuity zones into structures to generate the skeleton map (Fig. 15c). A series of skeletonization and vectorization techniques (selecting line segments) were used to the findings to detect and recognize the linear features in the region (Fig. 15c). Figures (15a–c) show multiple intersection zones with NE–SW trending. Each skeleton line in Fig. 15c reflects weak (shear) zones over this direction. The structural control trends are the ENE, NE–SW, NNE, E–W, and NW–SE trends. Further examination of the skeleton map (Fig. 15c) delineates that the high-density structures are arrayed along with ENE, NE, E–W, and NW directions. The intersections of the detected lineaments can also be used to identify possible traps for possible hydrothermal fluids (*Shebl et al., 2021*). This assumption is confirmed by Well Rigwa-1 where the water temperature reaches 70 degrees Celsius as measured from site investigation (Fig. 15e). The collected line segments were used to construct the orientation entropy heat map (Fig. 15d). The map is connected with feature orientation variation



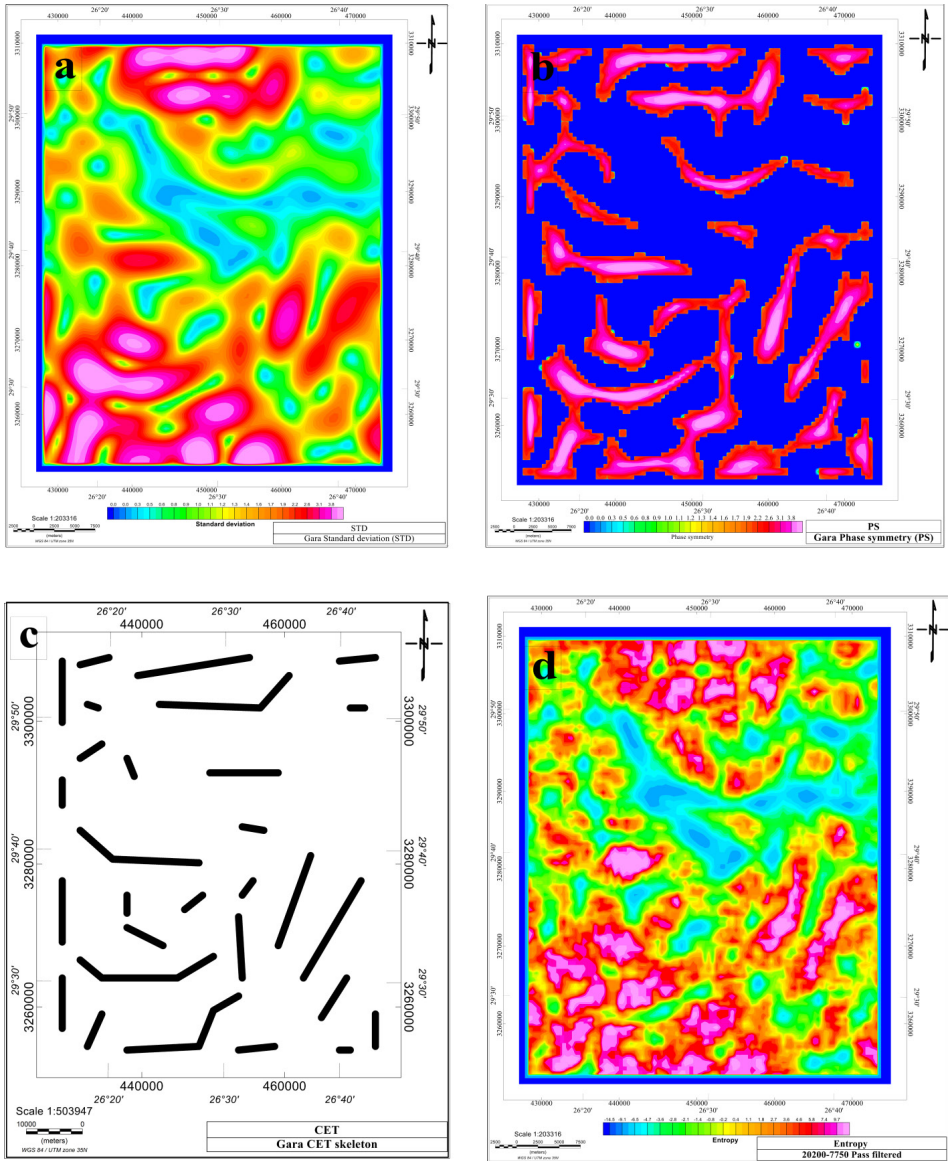


Fig. 15. a) Standard deviation (STD); b) phase symmetry (PS); c) skeletonization; d) entropy; and e) temperatures distribution through the wells.

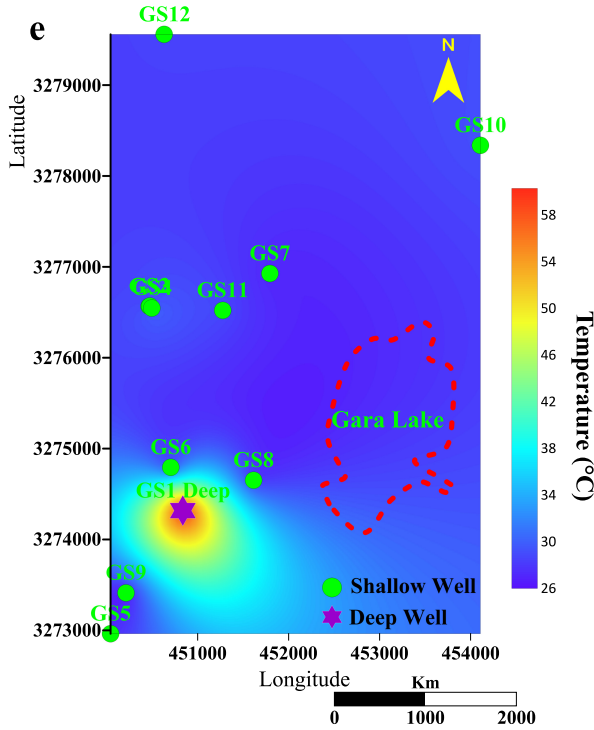


Fig. 15. Continued from the previous page.

(lineaments including crossings and intersections), facilitating the determination of structural complexity zones.

The result of the skeletonization over RTP and residual maps over the study area is shown in Figs. 16 and 17 where their main high anomalies toward the eastern, western, and northern parts of the area can be distinguished. Each one of these anomalies is controlled with the skeleton structure trends. Possible faults/contacts separate these anomalies as indicated in Fig. 16. The rose diagram of these trends diagrams reveals two major structural trends with varying intensities and lengths (Fig. 18). The NE–SW, NNE–SSW, and E–W trends, as indicated by magnetic data, depict the most major tectonic trends impacting the investigated area. The other minor structural trends depicted on the rose diagrams, such as the NW–SE, are, however, less significant in this setting.

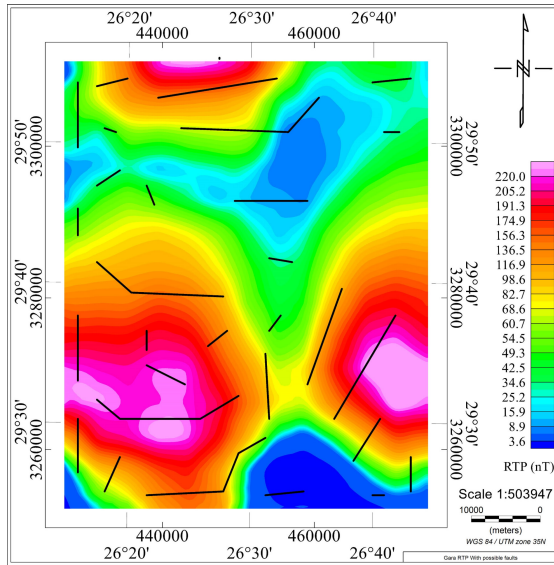
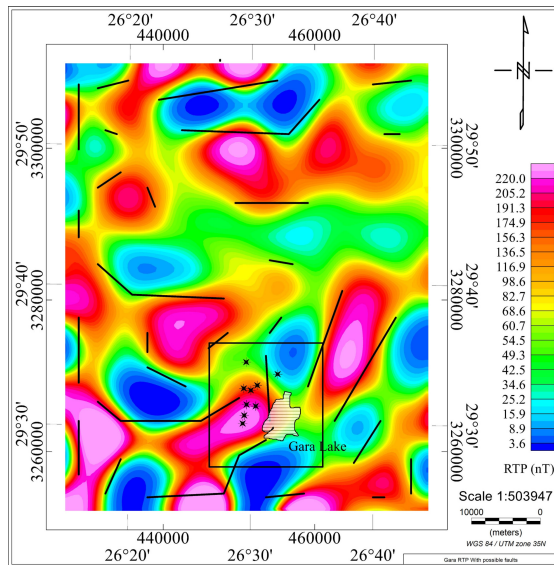


Fig. 16. Skeletonization as posted on the RTP map of the study area.



\* Water Sample

Fig. 17. Skeletonization with Residual RTP map of the study area.

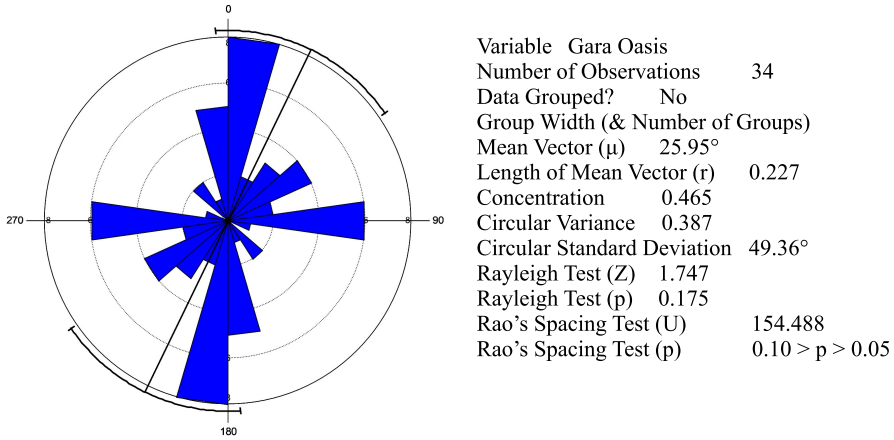


Fig. 18. Rose diagram showing the structure trends in the study area and its statistical analysis.

## 4.2. Hydrogeochemistry

### 4.2.1. Spatial distribution

The pH values range from 7.3 to 7.9, indicating moderately basic water, according to the chemical analyses (Table 1). According to *Bis (1998)*, all of the water samples had pH levels between 6.5 and 8.5, which was within the permitted range. The spatial distribution map of pH (Fig. 19a) shows higher values (slightly alkaline) at (Western and NW) parts that represent lower salinity (TDS) as in (Fig. 19c) wherever lower values of PH recorded at (Eastern and SE) parts including higher salinity close to Gara Lake. Water's electrical conductivity (EC) ranges from 6430 to 10910 ( $\mu\text{s}/\text{cm}$ ) and is a measurement of its capability to transport an electric current. In general, the water EC shows an increment in (Eastern and SE) parts close to Gara Lake and a decrease in (Western and NW) parts Fig. 19b. Freshwater (TDS < 1500 mg/l), brackish water (1500 to 5000 mg/l), and saline water (TDS > 5000 mg/l) are the three main kinds of total salinity, according to *Chebotaiev's* categorization (*Chebotaiev, 1955a,b,c*). The investigated aquifer's groundwater salinity (TDS) refers to brackish to saline water (*Gad et al., 2018; Aly, 2015; Abo El-Fadl et al., 2015*) with salinity contents varying from 3500 to 6500 mg/l (Fig. 19c). This salinity could be related to the

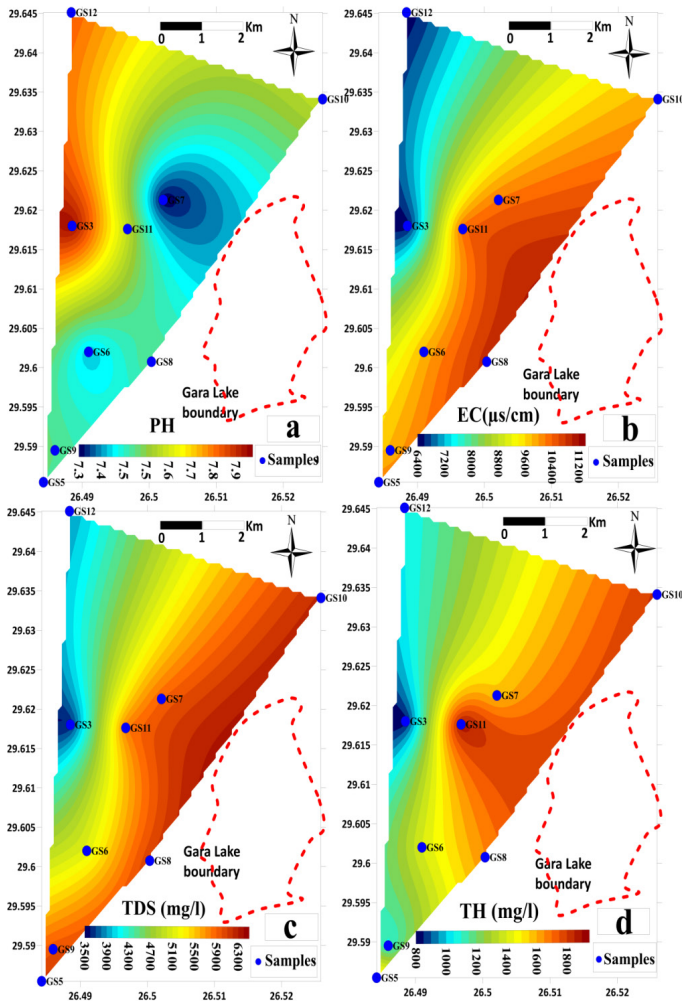


Fig. 19. The sample locations, and geospatial concentration of (a) PH, (b) EC, (c) TDS, and (d) TH in the research area is depicted on maps.

shallow depth of the wells that stimulates the performance of evaporation, as the rainfall is low (45 mm/year) (Abo El-Fadl et al., 2015). The dissolution of gypsum streaks associated with limestone rocks is also thought to be related to the salt content (Yousef, 2010 and Guindy, 2000). TDS spatial distribution map in Fig. 19c shows an increase in Eastern and SE parts and

a decrease in Western and NW parts.

The total hardness (TH) may be calculated using the following equation, according to *Todd (1980)*, *Hem (1985, 1989)*, and *Ragunath (1987)*:

$$\text{TH (mg/l)} = 2.497 \text{ Ca}^{2+} + 4.115 \text{ Mg}^{2+}. \quad (2)$$

Figure 19d and Table 1 show the total hardness of the water samples obtained, ranged from 817.244 to 1893.459 (mg/l) as  $\text{CaCO}_3$ . Its values display under the (very hard) category related to the increase in salinity (*Abo El-Fadl et al., 2015*), reflecting the limestone dissolution which led to salinity increase as explained before. Spatially, pH, EC, TDS, and TH concentrations increased toward the east where Gara Lake is located. This is essentially associated with the consequence of leaching and dissolution of dissolvable salts reaching to the increase of hardness (TH) with the appropriate value to the impact of NaCl concentration (influence of ionic strength) on increasing solubility of  $\text{Mg}^{2+}$  and  $\text{Ca}^{2+}$  in water (*Freeze and Cherry, 1979; Hem, 1989*).

The major ions Na, Ca, Mg, K, Cl,  $\text{HCO}_3$ , and  $\text{SO}_4$  describe the total mineralization of most groundwater. As shown in Table 1, the highest recorded concentration among cations is Na and among anions is Cl, while arrangement discerningly based on the percentage of concentrations for cations is  $\text{Na} + \text{K} > \text{Ca} > \text{Mg}$  while Anions  $\text{Cl} > \text{SO}_4 > \text{HCO}_3$ . As shown in (Figs. 20a, b, c, e, and g), following the general TDS increasing trend, Ca, Na, Cl, Mg, and  $\text{HCO}_3$  are increased toward the eastern part with southern and SW part for (Ca, Na, Cl, and  $\text{HCO}_3$ ), elsewhere Northern and NW for Mg. The maximum concentrations of these elements (420.6, 1850, 3050, 217.8, and 280.6 mg/l, respectively) were noticed in samples GS11 except Na which gets its maximum at sample GS9. On the other hand, the concentration of K and  $\text{SO}_4$  (Figs. 20d and f) increased toward the North-eastern part for both K and  $\text{SO}_4$  in addition to NE for  $\text{SO}_4$  direction where the maximum concentrations of both elements were recorded (473 and 1273.5 mg/l). Sample GS3 which located in the western part is represents the lowest concentrations of Ca, Na  $\text{SO}_4$ , and Cl (139.4, 1040, 360, and 1750 mg/l, respectively) while the lowest concentrations of Mg and K (60.7 and 41 mg/l) are represented by sample GS9 in the southern part. The lowest concentration of  $\text{HCO}_3$  (183 mg/l) was encountered in the north-western part where sample G12 is located.

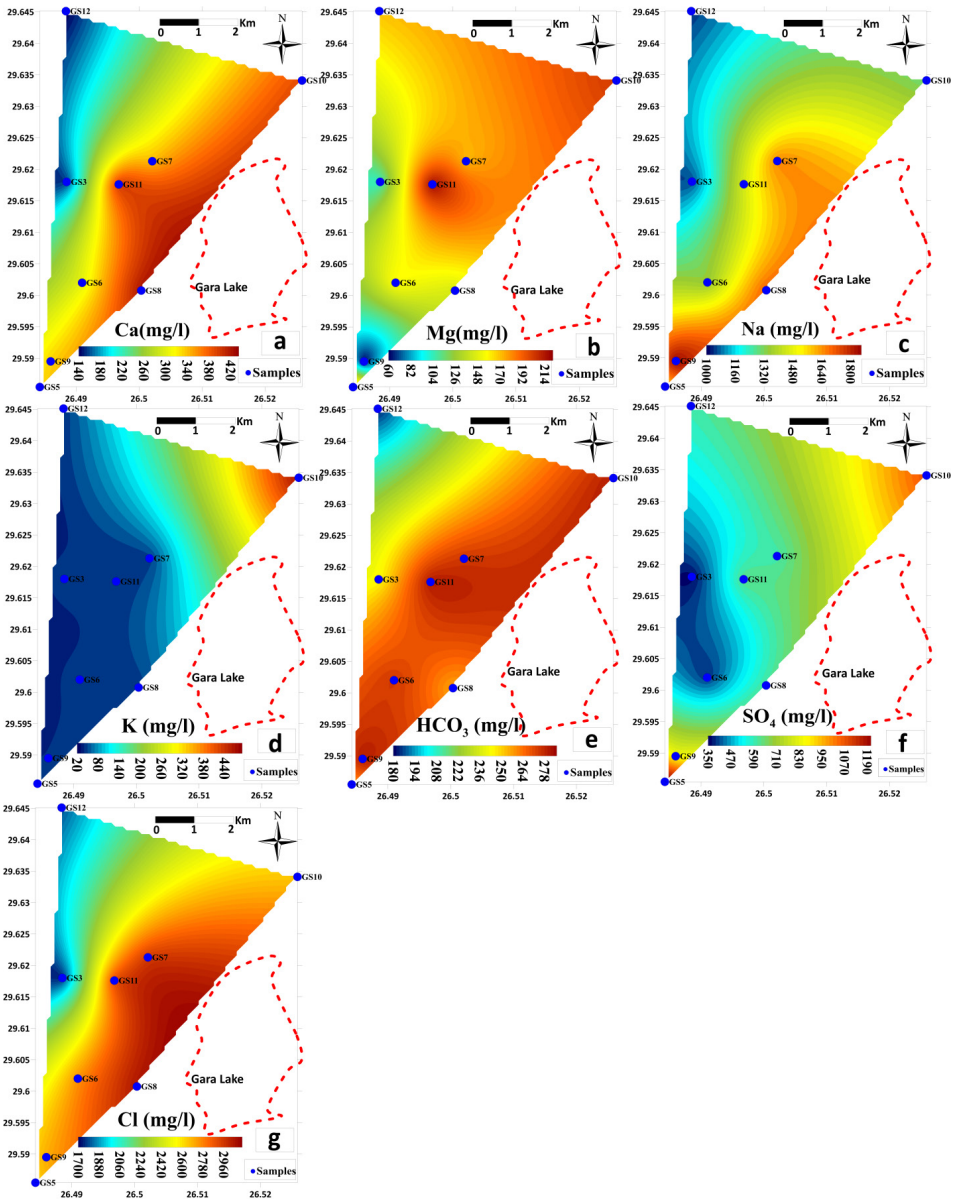


Fig. 20. The concentrations of the main ions (mg/l) in the investigated area (a) Ca; (b) Mg; (c) Na; (d) K; (e) HCO<sub>3</sub>; (f) SO<sub>4</sub>; and (g) Cl.

**4.2.2. Samples classifications**

**Cluster analysis (CA)**

Hierarchical clustering is the most widely used in environmental sciences, according to *Davis (1986)* and *Salem et al. (2015)*, and is regularly used in the organization of hydrogeochemical data. Using hierarchical cluster analysis, CA is used to categories estimated groundwater properties into groups or clusters depending on their similarity or differences that exist in data set variations (*Abdel-Gawad et al., 2020; Salem and Osman, 2017; Salem and El-Horiny, 2014*). When two items belong to the same group, their point of connection is maximum; otherwise, it is minimum. The distance between samples is considered as a measure of similarity in hierarchical cluster analysis (*Vega et al., 1998*).

Based on these hydrochemical compositions, collected samples were classified into three groups as shown in Fig. 21a dendrogram. Also using cluster analysis, ion associations were distinguished into three groups as presented in Fig. 21b dendrogram. The dendrogram in Fig. 21a reveals that G1 samples are related to G2, and G3 at a significant distance, this means that two samples (GS3 and GS12) can be differentiated from the other groundwater samples hydrogeochemically. G2 and G3 are highly associated groundwater groups that indicate hydrogeochemical variations from G1. With sequences of Na > Mg > Ca and Cl > SO<sub>4</sub> > HCO<sub>3</sub>, Group G1 has the lowest average TDS (3740.5 mg/l). Regarding sequences of Na > Ca > Mg and Cl > SO<sub>4</sub> > HCO<sub>3</sub>, groups G2 and G3 have average TDS values of 3598 and 6230 mg/l, respectively (Table 2). The samples from group 1 are situated in the western and north-western parts of the region, while the samples from the other two groups are concentrated in the central and western parts.

Schoeller diagrams are used to describe the water chemical categories of the sample groups (Figs. 22a, b, and c). In general, all of the groups re-

Table 2. The average composition of the hydrochemical parameters of the three sample groups. TDS (mg/l) and ions (meq/l).

Group	TDS	K	Na	Mg	Ca	Cl	SO <sub>4</sub>	HCO <sub>3</sub>
G1	3740.5	1.14102	45.65217	11.38005	7.38603	50.71428	9.99416	3.5
G2	5820.25	3.89102	61.41304	15.89235	17.77049	78.03571	17.5432	4.475
G3	5991.33333	1.11111	75.36231	10.50888	18.25	82.85714	14.3361	4.43333



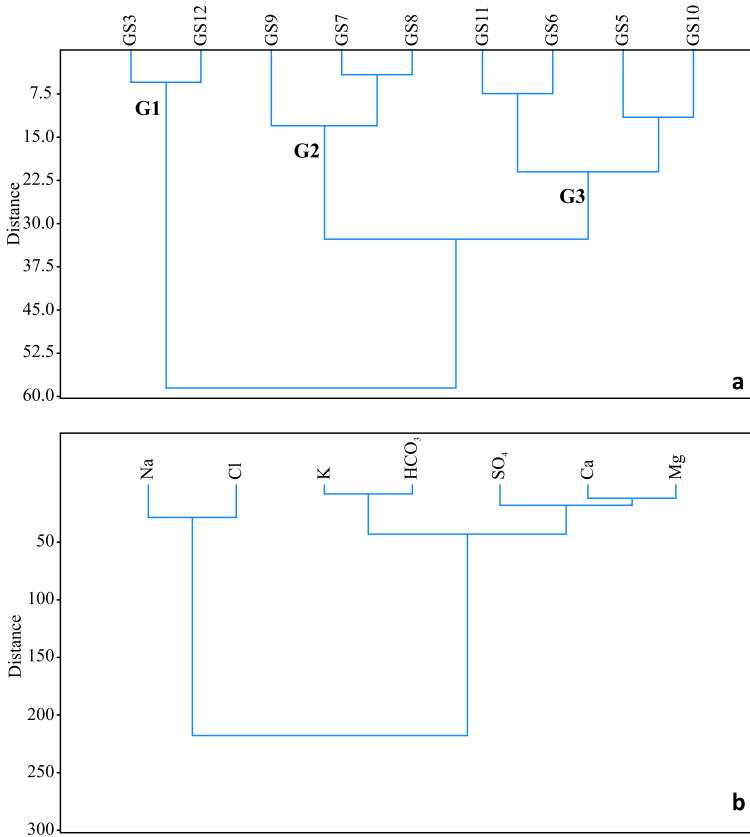


Fig. 21. Dendrograms show the groundwater samples groups (a) and the ion associations (b) based on ion concentrations in meq/l.

vealed that the predominant ions in the groundwater were Na and Cl. This might be due to evaporation or halite dissolution with the upward flow of groundwater via the fractures from the deeper aquifer, Nubian sandstone aquifer to the shallower aquifer, fractured shallow Miocene limestone aquifer (*El Hossary, 2013; Aly, 2015*). Three ion associations were distinguished Na-Cl, K-HCO<sub>3</sub>, and SO<sub>4</sub>-Mg-Ca (Fig. 21b). Such ion associations reflect the possible hydrochemical processes affecting the studied groundwater. Na-Cl association indicates evaporation and halite dissolution, K-HCO<sub>3</sub> represents the organic matter decay and fertilizers application and SO<sub>4</sub>-Ca-Mg association could be related to sulphate dissolution.

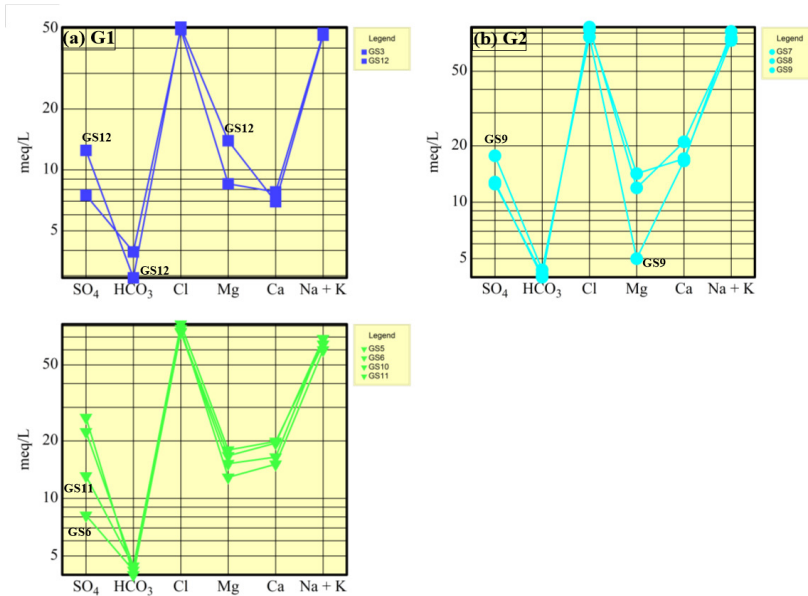


Fig. 22. Schoeller diagrams of the gathered groundwater samples, each set of samples representing a chemical type.

### Piper Diagram

On a Piper trilinear, the hydrochemical data of the categorized groundwater samples were described (*Piper, 1944*, and Fig. 23). Piper diagrams are a significant tool in identifying water types collected from various groundwater resources areas based on the ionic structure of distinct water samples (*Salem and Bayumy, 2016; Al-Ahmadi, 2013; Al-Omran et al., 2013; Semerjian, 2011; Baba et al., 2008*). The piper diagram shows that all of the recorded samples graphed within the Na-Cl category sub-area, with Na as the predominant cation and Cl as the predominant anion in the investigated groundwater, as shown in Fig. 23. All samples are grouped and gathered in the alkaline water with principal sulphate with chloride domain and sodium with potassium domain, indicating that the groundwater samples correspond to the Na, K, Cl, and SO<sub>4</sub> facies, indicating the dominance of alkali over alkaline earth ( $Na + K > Ca + Mg$ ) and strong acids over weak acids ( $Cl + SO_4 > HCO_3$ ), according to piper’s diamond field classifications. This is mostly attributed to the evaporation of gypsum and halite as ma-

rine sediments related to Miocene limestone as aquifer material and/or the dissolving of halite and gypsum as marine deposits (Aly, 2015; Gad et al., 2018; Abo El-Fadl et al., 2015; El Hossary, 2013).

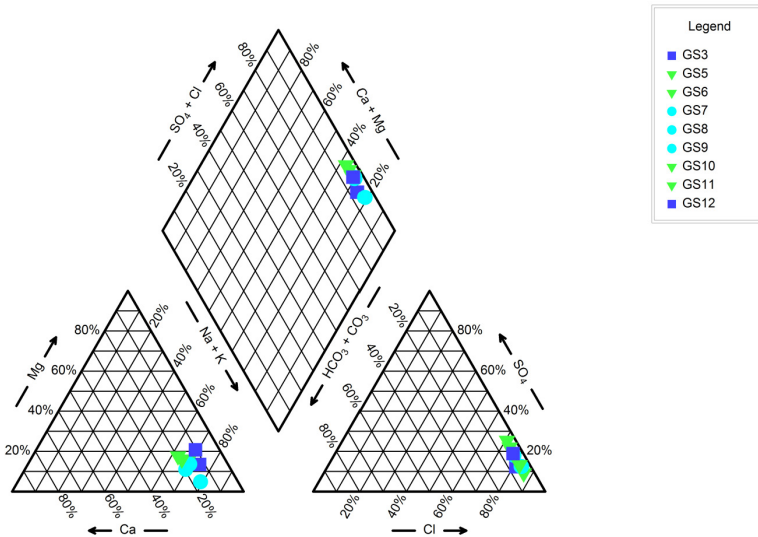


Fig. 23. The hydrochemical type of the obtained groundwater samples is depicted in a Piper diagram.

### The Diagram of Sulin

According to Sulin’s diagram (Fig. 24), three water types were distinguished. The greater salinity of the samples, which exceeds 6230 mg/l, confirms a recent marine ( $MgCl_2$  type) water origin (samples GS3, GS5, GS10, and GS12). When  $(rCl - r(K + Na)) / rMg < 1$  for this water type, indicating that there is no additional Cl to interact with Ca (Abdelazeem et al., 2020). The increased salinity of the samples establishes brine water ( $CaCl_2$  old marine water), which reaches 6102 mg/l and is expressed at samples (GS6, GS7, GS8, and GS11). When  $(rCl - r(K + Na)) / rMg > 1$  in this water type, indicates that Cl can react with Ca to create  $CaCl_2$  (Abdelazeem et al., 2020). The continental water (deep meteoric water,  $Na_2SO_4$ ) is represented by only one sample (GS9). This meteoric water type might be related to groundwater generated previous to improvement activities, when soil salinity is the predominant factor of groundwater constituents (Salem et al., 2015).

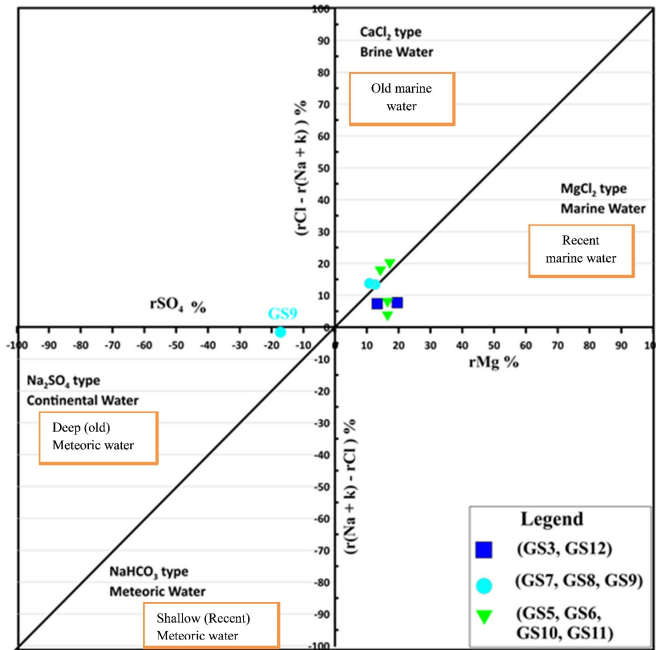


Fig. 24. the genetic types of the investigation area’s shallow groundwater are depicted in Sulin’s diagram.

### 4.2.3. Hydrogeochemical processes

#### Gibbs diagrams

The ratios of  $Na + K / (Na + Ca + Mg)$  and  $Cl / (Cl + HCO_3)$  as a consequence of TDS are depicted in Gibbs’ diagrams (Fig. 25a, b). Precipitation dominance, rock dominance, and evaporation dominance are all characteristics of main resources of dissolved chemical components that may be evaluated using these diagrams (*Gibbs, 1970*). The Gibbs diagram (Fig. 25a, b) indicates that the major contributor of Na and Cl is evaporation. Moreover, Evaporation enhances salinity degree by causing an increase in Na and Cl concentrations, as well as an increase in TDS levels. The concentrations of ions produced by mineral dissolution develop significantly as a result of evaporation, resulting in higher salinity (*Subba Rao, 2006; Kumar et al., 2014; Aly, 2015*).

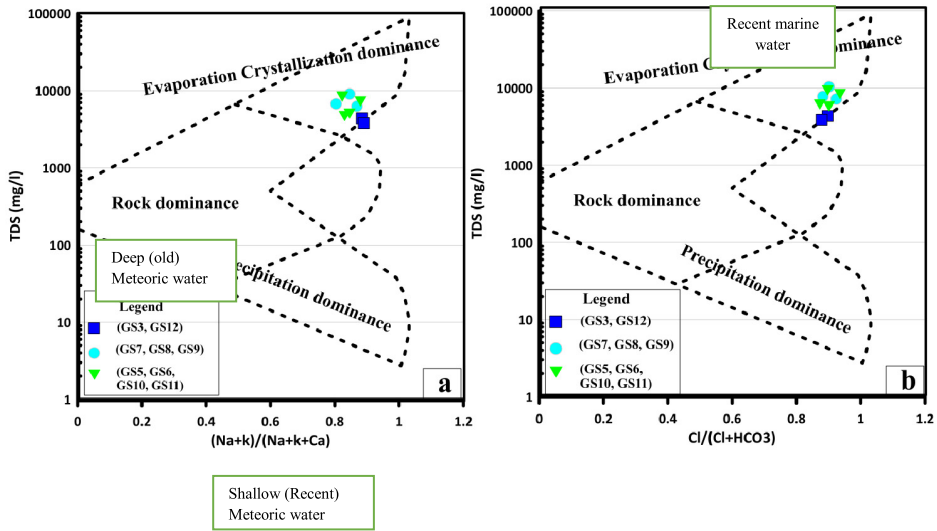


Fig. 25. The hydrogeochemical processes in the examined groundwater aquifer are shown using Gibbs diagrams (a, and b). TDS and ion concentrations are measured in milligrams per liter (mg/l).

### Relationships between TDS and ions

Figure 26a-g illustrates the correlations of TDS with the main ions Ca, Mg, Na, k, HCO<sub>3</sub>, SO<sub>4</sub>, and Cl, while Table 3 includes the coefficients of correlation values (r). The most significant ions indicating the primary features of salinity are Ca, Na, HCO<sub>3</sub>, and Cl. The corresponding plots of TDS correlations with Ca, Na, HCO<sub>3</sub>, and Cl depicted in Fig. 26a, c, e, and g have correlation coefficients equal to 0.96, 0.81, 0.82 and 0.97, respectively (Table 3). The other elements Mg, K, and SO<sub>4</sub> don't affect the current groundwater salinity where their relationships with TDS show week order (Table 3). In TDS-Na and TDS-Cl relationships (Fig. 26c and g) samples are clustered around the evaporation line suggesting that the present groundwater's Na and Cl concentrations are controlled by the evaporation process. In these graphs, samples are plotted across the evaporation line (Fig. 26a, e, and f) revealing that the excess of Ca, HCO<sub>3</sub>, and SO<sub>4</sub> could be related to mineral dissolution. In contrast, Mg and K (Fig. 26b, and d) are plotted below the evaporation line which might be due to mineral precipitation.

Table 3. Matrix of correlation coefficients between dissolved ion concentrations.

	PH	TDS	EC	K	Na	Mg	Ca	Cl	SO <sub>4</sub>	HCO <sub>3</sub>
PH										
TDS	-0.56134									
EC	-0.57515	0.9991								
K	-0.18064	0.13581	0.13435							
Na	-0.42302	0.81598	0.81727	-0.19011						
Mg	0.021322	0.21188	0.22807	0.35534	-0.24448					
Ca	-0.55756	0.96031	0.96203	0.2878	0.72807					
Cl	-0.62597	0.97841	0.9829	0.056965	0.80924	0.25226	0.9421			
SO <sub>4</sub>	0.15363	0.3623	0.3691	0.45112	0.33375	0.26023	0.39957	0.24227		
HCO <sub>3</sub>	-0.39113	0.82332	0.80322	0.25792	0.6121	0.023007	0.76696	0.75052	0.19496	
> 0.7 is strong (green color), 0.5–0.7 implies moderate (red color) and < 0.5 is week (black)										

### Ionic relationships

The correlations between the various main ions are extremely important for determining the origin of salts and groundwater hydrogeochemical processes, as well as for correlating various water characteristics (Hem, 1989). As a result, correlation coefficients (Table 3) were computed, and scatter binary plots between distinct ionic pairings were generated (Fig. 27). The origins of salinity in the area may be seen in the plot of the Na with Cl correlation (Fig. 27a). The strong interaction involving Na and Cl ( $r = 0.809$ ) reveals that each ion can be created within the same sources, which might include dissolution of halite, evaporation, and confined old saline water in sediments (Abdelazeem et al., 2020; Barzegar et al., 2017; Narany et al., 2014).

The plot Ca/SO<sub>4</sub> (Fig. 27b) is shown with week correlation ( $r = 0.33375$ , Table 3), while the samples are distributed around the line of unity, which indicates the source of this groundwater samples are formed from each of Ca and SO<sub>4</sub> by equality. The plot of Ca with Cl helps in determining how groundwater composition changes as a result of the dissolution of salt minerals including anhydrite, gypsum, dolomite, and calcite (Abdelazeem et al., 2020; Salem et al., 2015). Ca and Cl ions have a very strong positive connection ( $r = 0.94$ , Table 3, and Fig. 27c), and all samples are plotted higher than the 1:2 line, indicating that Cl concentration is greater than Ca concentration. The plot Na/HCO<sub>3</sub>, and Cl/HCO<sub>3</sub> relationships (Fig. 27d and e) are shown with an intermediate and strong correlation ( $r = 0.6121$

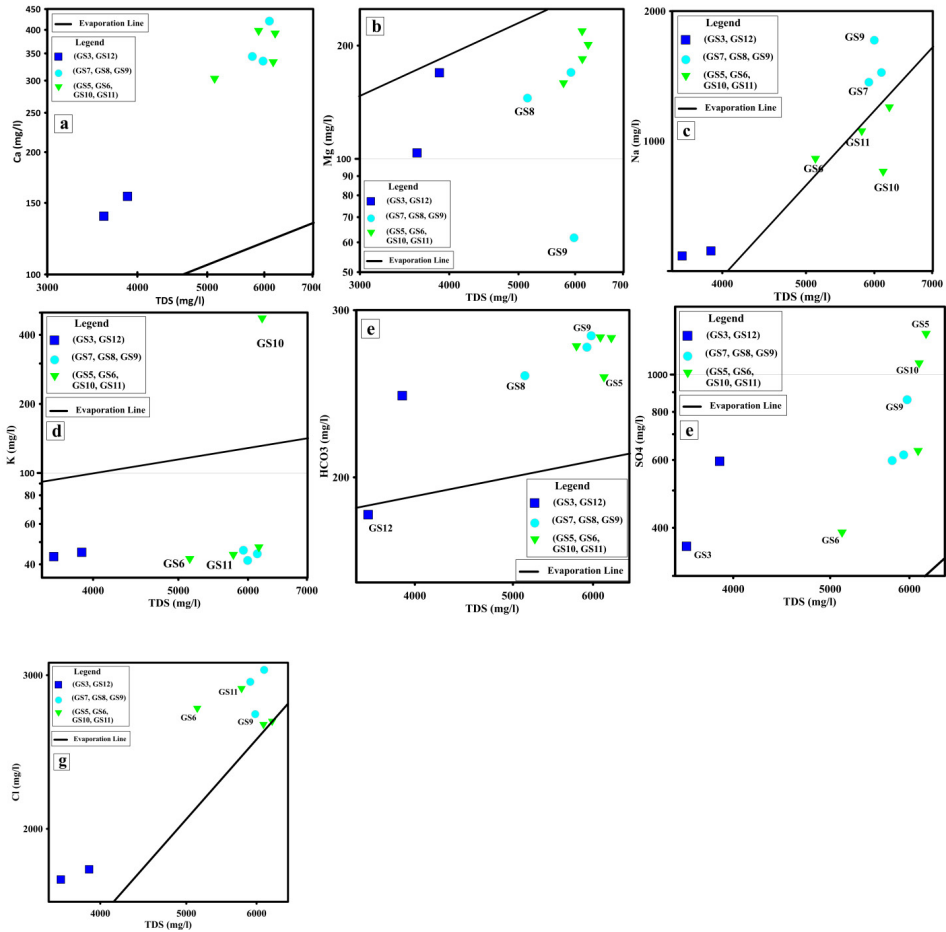


Fig. 26. The relationship between Total Dissolved Solids (TDS) and Ions concentrations (a-g).

and 0.75052, respectively). The samples are plotted lower than the line of unity where Na and Cl concentrations are higher compared to that of  $\text{HCO}_3$ . The plot Na/Ca ratio (Fig. 27f) is shown with a strong coefficient ( $r = 0.72807$ ) and samples are distributed lower than the line of unity toward the Na concentration, which indicates the effect of the exchange of ions between Na and Ca (Salem et al., 2015). The Ca/ $\text{HCO}_3$  plot in (Fig. 27g) shows a strong relation ( $r = 0.76696$ ), while the samples are distributed lower than

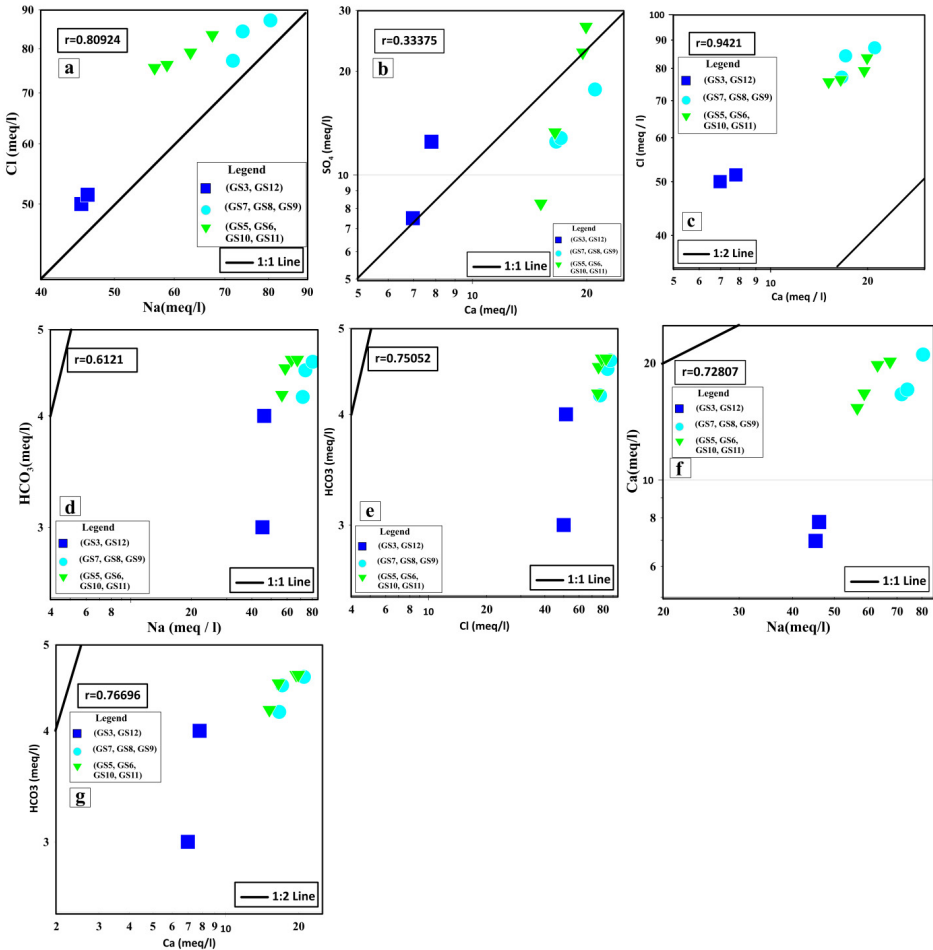


Fig. 27. The hydrogeochemical processes that occurred in the investigated groundwater region were evaluated using ionic relationships.

the 1:2 line where excess Ca concentration is noticed. This indicates the dissolution of calcite and the effect of the ion exchange process (Salem et al., 2016).

### Ion exchange

One of the water-sediment interactions that have a significant impact on the primary ion compositions of groundwater is ion exchange (Xiao et al.,



2012). In seepage zones, ion exchange interactions between clay minerals and groundwater are essential (Salem et al., 2015). Ion exchange occurs in the configurations containing a plot of  $((Ca + Mg) - (SO_4 + HCO_3))$  with  $(Na - Cl)$ , as shown in Fig. 28. Groundwater is not affected by ion exchange when samples plot closer to zero toward the  $y$ -axis after subtracting Cl from Na and assuming that all Cl originates from NaCl. The amount of Ca and Mg is given by the corresponding dissolution of calcite, dolomite, and gypsum on the  $x$ -axis of  $((Ca + Mg) - (SO_4 + HCO_3))$ . Groundwater samples will plot on a direct line with a high correlation coefficient if exchange processes occur in the arrangement (Jankowski et al., 1998). Correlation coefficient ( $r = -0.83662$ ) of data from the research area depicted in (Fig. 28). As shown in Fig. 28, most of the considered samples except GS9 have an excess of Ca + Mg which could be obtained from replacing Na, indicating an ion exchange process. Sample GS9 has an excess of Na, which might be related to replacing (Ca + Mg). As a consequence, in the investigated groundwater, the ion-exchange process owing to water-rock interaction is a dominating component (Salem et al., 2016).

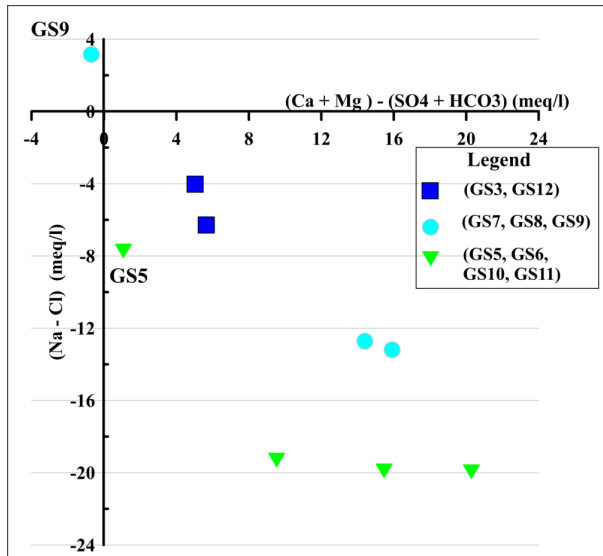


Fig. 28. The ion exchange mechanisms in the groundwater samples examined are depicted in a binary diagram.

Ca + Mg concentrations have no significant relationship with  $\text{HCO}_3 + \text{SO}_4$  ( $r = 0.4487522$ ), as shown in the Fig. 29a. The interaction between  $\text{Na} + \text{k} + \text{Ca} + \text{Mg}$  and  $\text{HCO}_3 + \text{SO}_4$  ( $r = 0.5688281$ , Fig. 29b) is, on the other hand, significant. These two relationships indicated that Ca and Mg aren't just generated through the degradation of calcite, gypsum, anhydrite, and dolomite, but also from other weathering of mineral and ion exchange with Na (*Abdelazeem et al., 2020; Salem and Osman, 2017; Salem et al., 2015*). Ca and Mg were eliminated from the solution in samples GS5 and GS9, which might be associated to calcite and dolomite precipitation owing to sulphate (*Aly, 2015; Salem et al., 2015; Salem and Osman, 2017; Abdelazeem et al., 2020*).

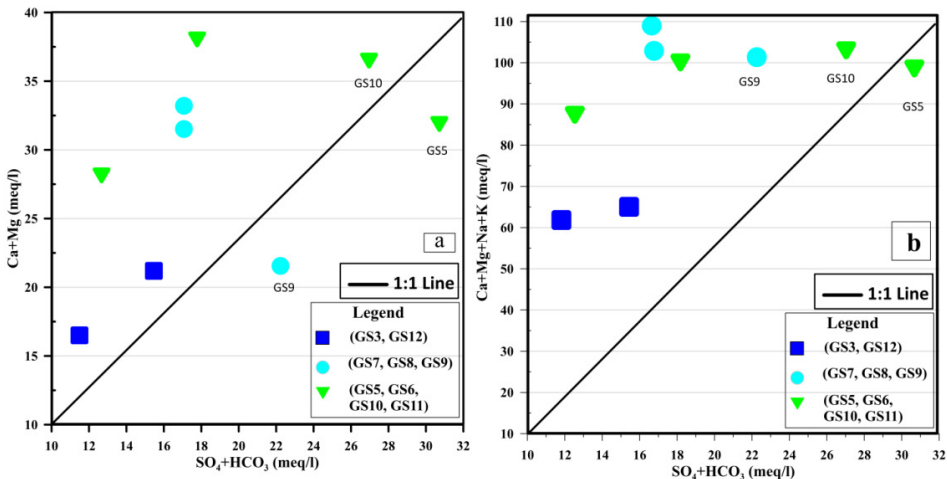


Fig. 29. Relationships illustrating how sodium replaces Ca and Mg in dissolved sulphate and carbonate minerals to create salts with  $\text{SO}_4$  and  $\text{HCO}_3$ .

### 5. Discussion and conclusion

The extensive systems of faults impacting and controlling the aquifer of the GO are represented by aeromagnetic data analysis. A fault contact system controls the structure of shallow and deep aquifers that is evident from the spatial filters applied to the data and its attributes as standard deviation (STD), Phase symmetry (PS), CET skeleton, Entropy, Phase congruency, amplitude thresholding, Skeletonization, and residual separation (bandpass

filter). By using potential aeromagnetic field data, the subsurface structures are delineated and it is now possible to explain the complex structure of faults/contacts that impact and regulate the GO groundwater aquifer flow. The common extracted trends are ENE, NE, NNE, NW, and E–W. The rose diagram revealed the two most common trends of the Phase symmetry (PS) and CET skeleton maps were NE–SW, NNE–SSW, ENE–WSW and, E–W, with minor trends in NW–SE. These faults and fractures, which extend along the edges of the Gara depressions, control and regulate underground water movement in all sides as well as in adjacent sedimentary basins (potential water carriers). This is represented in Miocene Carbonate, a thick and thin shallow aquifer near the surface represented in the study area by the fresh to slightly brackish water of the Dolomite calcareous limestone rock. Hydrochemically, the Miocene Dolomite limestone was saturated with fresh to slightly brackish water of the near-surface groundwater interested aquifer in the researched area, and the overburden strata were classified into about six layers. Groundwater, a significant source of water in Egypt's western desert, is suffering from serious quantity and quality issues. Scarcity of water, in combination with the generally arid climate and the overuse of soils for agriculture, results in serious water quality issues. In GO, water salinity, a major indication of irrigation water quality, was expected to be highest above the permissible limit in most of the wells investigated, and it continues to rise with time. Problems with salinity, chloride and sodicity render this water inappropriate for irrigation and have a harmful impact on agricultural operations in GO. In general, the water collected from the GO reflects shallow groundwater samples from the Miocene aquifer, and its salinity ranged from moderate to high. All of the wells in the research region exhibited bicarbonate and pH levels that were within permissible limits. Sodium, magnesium, and chloride, on the other hand, were the most abundant ions in GO. The type of water that predominates in the Gara research area is NaCl, which is mostly attributable to the geology of the area, which contains halite. It was also obvious that some areas had distinct iron toxicity, such as sodium chloride. The deep artesian wells of Nubian sandstone aquifers, on the other hand, were adequate for irrigation of all sensitive crops, since groundwater is GO's only supply of water. In the study areas, shallow well water salinity varies from 3598 to 6230 mg/l (ppm), indicating that all water samples from shallow aquifers are salinity-

high. The average in shallow aquifers was **9222.72  $\mu\text{s}/\text{cm}$** , with a range of **6430 to 10910  $\mu\text{s}/\text{cm}$** . The salinity problem is regarded as the significant complexity facing agriculture in the Gara agro-ecosystem since most of the groundwater utilized for irrigation is taken from shallow aquifers, which are characterized by high salinities. According to Sulin's diagram, three water types were distinguished. Recent marine ( $\text{MgCl}_2$  type) water origin that is verified by the samples' greater salinity reaches 6230 mg/l (samples GS3, GS5, GS10, and GS12). Brine water ( $\text{CaCl}_2$  old marine water) which is established by the higher salinity of the samples reaches 6102 mg/l and is expressed at samples (GS6, GS7, GS8, and GS11). The continental water (deep meteoric water,  $\text{Na}_2\text{SO}_4$ ) is represented by only one sample (GS9). While Gibbs's diagram illustrates that the evaporation process is the principal source of Na and Cl. Evaporation enhances salinity via increasing Na and Cl concentrations, which is associated with an increase in TDS. TDS-Na and TDS-Cl relationships demonstrate that samples are concentrated around the evaporation line, revealing that the evaporation process is regulating Na and Cl concentrations in present groundwater. In the plot of the Na with Cl correlation, the correlations between the different main ions reveal the source of salinity in the area. The considerable improvement among Na and Cl ( $r = 0.809$ ) indicates that either ion might come from the same supply, which could be evaporation, degradation of halite, or previous trapped saline water in the sediments. To leach and eliminate salts from the soil profile and ultimately reconstruct the degraded agro-ecosystem, the study suggests utilizing deep fresh groundwater extracted from Nubian sandstone in a repeated sequence, combining or rotation approach with salty water from shallow Miocene aquifers.

**Acknowledgements.** The fieldwork, geologic site investigation, water sampling, are done through a Cairo University-funded Project: ID #17-269. We would like to thank our colleagues from Cairo University's Geophysics Department, Faculty of Science, for their help with the fieldwork, as well as their insight and knowledge, which significantly benefited the investigation.

**Funding.** This work's fieldwork is supported by a project funded by Cairo University, Project ID #17-269 (PI Prof. M. Gobashy).

**Conflicts of interest/Competing interests.** There are no conflicts of interest that are relevant to the content of this paper that the authors wish to declare.

**Data and materials are readily available.** Data sets created or analysed in the development of the current study are available from the corresponding author upon reasonable request.

**Code availability.** There is no code available in this work.

**Authors' contributions.** Gobashy M. M.: supplied the study's conception and design, acquisition of geophysical data, analysis and interpretation of magnetic data, authoring the paper, critically revising it for the importance of intellectual content, and final approval of the version to be submitted; Nazih M. M.: Carried out the geophysical and geochemical fieldwork (together with CU geophysics team), processing and interpretation with the help and supervision of the third author Zenhom S., and drafting the manuscript ( this interpretation is part of his M.Sc. thesis); Soliman K. S.: supplied the acquisition of data together with Nazih M. Abdelhalim A. was responsible for the Geologic part, and geologic fieldwork.

## References

- Abdelazeem M., Mekkawi M., Gobashy M. M., 2014: Subsurface structures using a new integrated geophysical analysis, South Aswan, Egypt. Arab J. Geosci., **7**, 12, 5141–5157, doi: 10.1007/s12517-013-1140-x.
- Abdelazeem M., Salem Z. E., Fathy M. S., Saleh M., 2020: Impact of lithofacies and structures on the hydrogeochemistry of the lower Miocene aquifer at Moghra Oasis, North Western Desert Egypt. Nat. Resour. Res., **29**, 6, 3789–3817, doi: 10.1007/s11053-020-09679-3.
- Abdelazeem M., Fathy M. S., Gobashy M., 2021: Magnetometric identification of sub-basins for hydrocarbon potentialities in Qattara Ridge, North Western Desert Egypt. Pure Appl. Geophys., **17**, 995–1020, doi: 10.1007/s00024-021-02678-2.
- Abdel-Gawad A. M., El Abd E. A., Gedamy Y. R., 2020: Geological characteristics of shallow groundwater aquifer and its relation to hydrochemical features and bacteriological pollutants in Siwa Oasis, Egypt. Int. J. Environ., **9**, 2, 117–147, doi: 10.36632/ije/2020.9.2.8.
- Abdelrahman E. M., Abdelazeem M., Gobashy M., 2019: A minimization approach to depth and shape determination of mineralized zones from potential field data using the Nelder-Mead simplex algorithm. Ore Geol. Rev., **114**, 103–123.
- Abdel-Rahman M. A., Embaby N. S., EL-Etr H. A., Mostafa A. R., 1980: Some geomorphological aspects of Siwa region. Geol. Geomorph. Studies Egypt. Desert Ain Shams Univ., 17–18.
- Abdulrahman A., Ahmad D. S., Muhammad A. U., 2017: Evaluation of soil corrosivity and aquifer protective capacity using secondary geoelectric parameters across Gombe metropolis in North-eastern Nigeria. Agric. Bus. Technol. J., **15**, 29–51.
- Abo El-Fadl M. M., Wassel M. A., Sayed A. Z., Mahmod A. M., 2015: Egypt. Part I, Significance of the situation groundwater resources and future outlook. Int. J. Sci.

- Res., (IJSR), **4**, 10, 447–458.
- Al-Ahmadi M. E., 2013: Groundwater quality assessment in Wadi Fayd, Western Saudi Arabia. *Arab. J. Geosci.*, **6**, 247–258, doi: 10.1007/s12517-011-0337-0.
- Al-Garni M. A., El-Behiry M. G., Gobashy M., 2012: Geophysical survey for geological hazards assessment of Wadi Thuwal area, KSA: a case history. *Arab. J. Geosci.*, **5**, 1, 133–146, doi: 10.1007/s12517-010-0147-9.
- Al-Garni M. A., Hassanein H., Gobashy M., 2006: Geophysical investigation of groundwater in Wadi Lusab, Haddat Ash Sham area, Makkah Al-Mukarramah. *Arab. Gulf J. Sci. Res.*, **24**, 2, 83–93.
- Al-Garni M. A., Gobashy M., 2010: Ground magnetic Investigation of subsurface structures affecting Wadi Thuwal area, KSA. *J. King Abdulaziz Univ., Earth Sci., JKAU*, **21**, 2, 167–193, doi: 10.4197/ear.21-2.7.
- Al-Omran M. A., El-Maghraby S. E., Aly A. A., Al-Wabel I. M., Al-Asmari Z. A., Nadeem M. E., 2013: Quality assessment of various bottled waters marketed in Saudi Arabia. *Environ. Monit. Assess.*, **185**, 8, 6397–6406, doi: 10.1007/s10661-012-3032-z.
- Aly A. A., 2001: Spatiotemporal monitoring and assessment of water resources in Siwa Oasis. MSc. Thesis, Faculty of Agriculture Saba Basha, Alexandria University, Egypt.
- Aly A. A., Benaabidate L., 2010: Salinity of water resources in the Siwa Oasis: Monitoring and diagnosis. In: Brikle P., Torres Alvarado I. S. (Eds.): *Water-rock interaction*. Taylor and Francis Group London, 363–365.
- Aly A. A., 2015: Hydrochemical characteristics of Egypt western desert oases groundwater. *Arab. J. Geosci.*, **8**, 9, 7551–7564, doi: 10.1007/s12517-014-1680-8.
- Aly A. A., 2020: Soil and groundwater salinization in Siwa Oasis and management opportunities. twenty year change detection and assessment. *Arid Land Res. Manag.*, **34**, 2, 117–135, doi: 10.1080/15324982.2019.1635662.
- Aly A. A., Abbas A. A., Benaabidate L., 2011: Hydrochemistry and quality of groundwater resources in Egypt: a Case study of the Egyptian Southern Oases. In: Scozzar A., El Mansouri B. (Eds.): *Water security in the Mediterranean region*. Springer, 239–254, doi: 10.1007/978-94-007-1623-0\_17.
- Aly A. A., Kishk F. M., Gaber H. M., Al-Omran A. M., 2016: Long-term detection and hydrochemistry of groundwater resources in Egypt: Case study of Siwa Oasis. *J. Saudi Soc. Agric. Sci.*, **15**, 1, 67–74, doi: 10.1016/j.jssas.2014.04.003.
- Araffa S. A. S., Gobashy M. M., Khalil M. H., Abdelaal A., 2021: Integration of geophysical techniques to detect geotechnical hazards: a case study in Mokattam, Cairo, Egypt. *Bull. Eng. Geol. Environ.*, **80**, 10, 8021–8041, doi: 10.1007/s10064-021-02388-y.
- Ayyad A. A., Ismail H. E., 1992: Stratigraphy and structure of the Mesozoic in the northwestern part of the Western Desert, Egypt. GPC Internal Report, ER 2483, 26 p.
- Baba A., Ereeş F. S., Hiçsönmez Ü., Çam S., Özdilek H. G., 2008: An assessment of the quality of various bottled mineral water marketed in Turkey. *Environ. Monit. Assess.*, **139**, 1-3, 277–285, doi: 10.1007/s10661-007-9833-9.

- Barzegar R., Moghaddam A. A., Tziritis E., 2017: Hydrogeochemical features of groundwater resources in Tabriz plain, northwest of Iran. *Appl. Water Sci.*, **7**, 7, 3997–4011, doi: 10.1007/s13201-017-0550-4.
- BIS, 1998: Drinking Water Specifications, Bureau of Indian Standards. IS: 10500.
- Chebotaev I. I., 1955a: Metamorphism of natural waters in the crust of weathering—1. *Geochim. Cosmochim. Acta*, **8**, 1-2, 22–48, doi: 10.1016/0016-7037(55)90015-6.
- Chebotaev I. I., 1955b: Metamorphism of natural waters in the crust of weathering—2. *Geochim. Cosmochim. Acta*, **8**, 3, 137–170, doi: 10.1016/0016-7037(55)90010-7.
- Chebotaev I. I., 1955c: Metamorphism of natural waters in the crust of weathering—3. *Geochim. Cosmochim. Acta*, **8**, 4, 198–212, doi: 10.1016/0016-7037(55)90053-3.
- Chidambaram S., Karmegam U., Prasanna M. V., Sasidhar P., Vasanthavigar M., 2011: A study on hydrochemical elucidation of coastal groundwater in and around Kalpakkam region, Southern India. *Environ. Earth Sci.*, **64**, 5, 1419–1431, doi: 10.1007/s12665-011-0966-3.
- Dahab K. A., 2004: Impact of the present groundwater exploitation system on the Nubia sandstone aquifer in Siwa Oasis, Western Desert, Egypt. 6th Intern. Conf. on Geochemistry, Alex. Univ., Egypt, 319–337.
- Davis J. C., 1986: Statistics and data analysis in geology, 2nd ed. John Wiley and Sons Inc, New York, 647.
- de Smet T. S., Nikulin A., Romanzo N., Graber N., Dietrich C., Puliaiev A., 2021: Successful application of drone-based aeromagnetic surveys to locate legacy oil and gas wells in Cattaraugus county, New York. *J. Appl. Geophys.*, **186**, 104250, doi: 10.1016/j.jappgeo.2020.104250.
- Dobrin M. B., Savit C. H., 1988: Introduction to geophysical prospecting. McGraw-Hill Book Co., Singapore.
- El Gammal E. A., 2010: Contributions to the geneses of continental waters in north western Egyptian Sahara using Landsat images. *Nat. Sci.*, **8**, 11, 35–43, doi: 10.7537/marsnsj081110.06.
- Egyptian general petroleum corporation (EGPC), 1989: Mineral, petroleum and groundwater assessment program, AID project, 263, 0105 and amendment No. 1. Reduction to the pole magnetic anomaly map.
- El Hossary M. F., 1999: Evaluation and management of groundwater resources in Siwa area with emphasis on the Nubian Sandstone aquifer. Ph.D. thesis, Fac. Sci. Ain Shams Univ., 143 p.
- El Hossary M. F. M., 2013: Investigating the Development Challenges to Siwa Oasis, Northwestern Desert, Egypt. *N. Y. Sci. J.*, **6**, 4, 55–61.
- El-Khoriby E. M., 1994: Sedimentology of Marmarica Formation (Middle Miocene) in Siwa Area, Northwest of Western Desert, Egypt. Ph.D. thesis, Moscow State Univ., Russia, 184 p.
- El-Sawy E. K., EldougDoug A., Gobashy M., 2018: Geological and geophysical investigations to delineate the subsurface extension and the geological setting of Al Ji'lani layered intrusion and its mineralization potentiality, Ad Dawadimi District, Kingdom of Saudi Arabia. *Arab. J. Geosci.*, **11**, 2, 32, doi: 10.1007/s12517-017-3368-3.

- Elzarka M. H., Radwan I. A. F., 1986: Subsurface geology of the Tertiary rocks of the northeastern district of the Western Desert of Egypt. *J. Afr. Earth Sci.*, **5**, 3, 285–319, doi: 10.1016/0899-5362(86)90018-7.
- Fergany E., Mekkawi M., Abdel Azeem M., Khalil A., 2015: Integrated geologic and geophysical studies of north unstable shelf seismicity, Egypt. *Arab. J. Geosci.*, **8**, 8, 5475–5490, doi: 10.1007/s12517-014-1620-7.
- Freeze R. A., Cherry J. A., 1979: *Groundwater*. Prentice Hall, Inc., Englewood Cliffs, New Jersey, U.S.A.
- Gad M., Dahab K., Ibrahim H., 2018: Applying of a geochemical model on the Nubian sandstone aquifer in Siwa Oasis, Western Desert, Egypt. *Environ. Earth Sci.*, **77**, 11, 401, doi: 10.1007/s12665-018-7580-6.
- General Petroleum Company (GPC), 1973: Evaluation of exploration activities and oil prospects in Siwa and adjacent areas, Western Desert, Egypt. GPC Internal Report.
- Geosoft OASIS montaj, 2015: 8.3.3 Mapping and Processing System, Geosoft Inc.
- Gibbs R. J., 1970: Mechanisms controlling world water chemistry. *Science*, **170**, 3962, 1088–1090, doi: 10.1126/science.170.3962.1088.
- Gimenez Forcada E., 2010: Dynamic of seawater interface using hydro chemical facies evolution diagram. *Groundwater*, **48**, 2, 212–216, doi: 10.1111/j.1745-6584.2009.00649.x.
- Gobashy M. M., Al-Garni M. A., 2008: High resolution ground magnetic survey (HRGM) for determining the optimum location of Subsurface Dam in Wadi Nu'man, Makkah Al Mukarammah, KSA. *J. King Abdulaziz Univ. Earth Sci.*, **19**, 1, 57–83, doi: 10.4197/ear.19-1.4.
- Gobashy M. M., Abdelazeem M., Abdrabou M., 2020: Minerals and ore deposits exploration using meta-heuristic-based optimization on magnetic data. *Contrib. Geophys. Geod.*, **50**, 2, 161–199, doi: 10.31577/congeo.2020.50.2.1.
- Gobashy M. M., Eldoudoug A., Abdelazeem M., Abdelhalim A., 2021a: Future development of gold mineralization utilizing integrated geology and aeromagnetic techniques: a case study in the Barramiya Mining District, Central Eastern Desert of Egypt. *Nat. Resour. Res.*, **30**, 3, 2007–2028, doi: 10.1007/s11053-021-09824-6.
- Gobashy M. M., Metwally A. M., Abdelazeem M., Soliman K. S., Abdelhalim A., 2021b: Geophysical exploration of shallow groundwater aquifers in arid regions: A case study of Siwa Oasis, Egypt. *Nat. Resour. Res.*, **30**, 5, 3355–3384, doi: 10.1007/s11053-021-09897-3.
- Guindy K. A., 2000: Assessment of groundwater resources in El Maghara area, central Sinai, Egypt. *Desert Inst. Bull. Egypt*, **50**, 2, 251–272.
- Hammad F. A., Aggour T. A., Shabana A. R., 2000: Water overflow in Siwa Oasis, the problem and the solutions. In: *Proc. 5th Intern. Conf. on Geol. Arab. World, Fac. of Sci., Cairo Univ.*, 2, 889–900.
- Hammer Ø., Harper D. A. T., Ryan P. D., 2001: PAST: Paleontological statistics software package for education and data analysis. *Palaeontol. Electron.*, **4**, 1, 4.
- Helaly A. S., 2017: Assessment of groundwater potentiality using geophysical techniques in Wadi Allaqi basin, Eastern Desert, Egypt – Case study. *NRIAG J. Astron. Geophys.*, **6**, 2, 408–421, doi: 10.1016/j.nrjag.2017.09.003.



- Hem J. D., 1985: Study and interpretation of the chemical characteristics of natural water. 3rd ed., U.S. Geological Survey, Water Supply Paper 2254, Washington D.C.
- Hem J. D., 1989: Study and interpretation of the chemical characteristic of natural water. 3rd ed., U.S. Geological Survey, Water Supply Paper 2254, 93, 116.
- Holden E.-J., Dentith M., Kovesi P., 2008: Towards the automated analysis of regional aeromagnetic data to identify regions prospective for gold deposits. *Comput. Geosci.*, **34**, 11, 1505–1513, doi: 10.1016/j.cageo.2007.08.007.
- Ibrahim S. A., 1991: Studies on groundwater possibilities in the northern part of the Western Desert Egypt. Ph.D. thesis, Cairo Univ., Cairo, Egypt, 292 p.
- Jankowski J., Acworth R. I., Shekarforoush S., 1998: Reverse ion-exchange in deeply weathered porphyritic dacite fractured aquifer system, Yass, New South Wales, Australia. In: Arehart G. B., Hulston J. R. (Eds.): *Proc. 9th Int. Symp. Water–Rock interaction*. Taupo, New Zealand, Balkema, Rotterdam 243–246.
- Kazatchenko A., Khalil N. A., Gavrilouk A., 1970: Geological technical project of prospecting works in Gibb Afia, Western Desert, Egypt. GPC Internal Report, ER 908, 15.
- Klute A., 1986: Methods of soil analysis. Part 1, 2nd ed. *Agron Monor* 9, ASA and SSSA, Madison, WI.
- Kumar K. S., Bharani R., Magesh N. S., Godson P. S., Chandrasekar N., 2014: Hydro-geochemistry and groundwater quality appraisal of part of south Chennai coastal aquifers, Tamil Nadu, India using WQI and fuzzy logic method. *Appl. Water Sci.*, **4**, 4, 341–350, doi: 10.1007/s13201-013-0148-4.
- Kwami I. A., Ishaku J. M., Bello A. M., Yusuf A., Abubakar U., Mukkafa S., 2018: Assessment of water quality index for the groundwater in Gombe and environs, North-East Nigeria. *IOSR J. Appl. Geol. Geophys.*, **6**, 5, 29–37, doi: 10.9790/0990-0605032937.
- Mohanaiah P., Sathyanarayana P., GuruKumar L., 2013: Image texture feature extraction using GLCM approach. *Int. J. Sci. Res. Publ.*, **3**, 5, 2250–3153.
- Moussa B. M., 2006: Miocene rocks and their impact on shallow groundwater, Siwa Oasis, Western Desert, Egypt. *Sedimentology of Egypt*, **14**, 117–142.
- Narany T. S., Ramli M. F., Aris A. Z., Sulaiman W. N. A., Juahir H., Fakharian K., 2014: Identification of the hydrogeochemical processes in groundwater using classic integrated geochemical methods and geostatistical techniques in Amol-Babol Plain, Iran. *Sci. World J.*, **2014**, 419058, doi: 10.1155/2014/419058.
- Ndatuwong L. G., Yadav G. S., 2014: Integration of hydrogeological factors for identification of groundwater potential zones using remote sensing and GIS techniques. *J. Geosci. Geomat.*, **2**, 1, 11–16, doi: 10.12691/jgg-2-1-2.
- Orabi S. A., Dawood M. G., Salman S. R., 2015: Comparative study between the physiological role of hydrogen peroxide and salicylic acid in alleviating the harmful effect of low temperature on tomato plants grown under sand-ponic culture. *Sci. Agric.*, **9**, 1, 49–59, doi: 10.15192/pscp.sa.2015.1.9.4959.
- Osman R., Orabi H., 2017: New findings in the Eocene stratigraphy of Siwa-El Qara stretch, north western desert, Egypt. *J. Afr. Earth Sci.*, **134**, 1–9, doi: 10.1016/j.jafrearsci.2017.04.033.

- Piper A. M., 1944: A graphic procedure in the geochemical interpretation of water-analyses. *Trans. Am. Geophys. Union*, **25**, 6, 914–928, doi: 10.1029/TR025i006p00914.
- Ragunath H. M., 1987: *Groundwater*. Wiley Eastern Ltd, New Delhi, 563 p.
- Raid S., 2001: Groundwater resources of Southwestern Desert of Egypt. *Ann. Meet. Geol. Soc., Egypt*, 17, Mars 2 (abstract).
- Rehman F., Abdelazeem M., Gobashy M. M., Harbi H. M., Rehman S., Abuelnaga H. S. O., 2019: Application of magnetic method to define the structural setting controlling the contaminated area of Wadi Bani Malik East Jeddah, Saudi Arabia. *Boll. Geofis. Teor. Appl.*, **60**, 1, 97–122, doi: 10.4430/bgta0269.
- RockWare AqQA software, 2011: Version AQC10664, <http://www.rockware.com>.
- Said R. (Ed.), 1990: *The Geology of Egypt*. A. A. Balkema, Rotterdam, Brookfield, 734 p., doi: 10.1201/9780203736678.
- Salem Z. E., El-Horiny M. M., 2014: Hydrogeochemical evaluation of calcareous eolianite aquifer with saline soil in a semiarid area. *Environ. Sci. Pollut. Res.*, **21**, 13, 8294–8314, doi: 10.1007/s11356-014-2735-9.
- Salem Z. E., Atwia M. G., El-Horiny M. M., 2015: Hydrogeochemical analysis and evaluation of groundwater in the reclaimed small basin of Abu Mina, Egypt. *Hydrogeol. J.*, **23**, 8, 1781–1797, doi: 10.1007/s10040-015-1303-9.
- Salem Z. E., Al Temamy A. M., Salah M. K., Kassab M., 2016: Origin and characteristics of brackish groundwater in Abu Madi coastal area, Northern Nile Delta, Egypt. *Estuar. Coast. Shelf Sci.*, **178**, 21–35, doi: 10.1016/j.ecss.2016.05.015.
- Salem Z. E., Bayumy D. A., 2016: Hydrogeological, petrophysical and hydrogeochemical characteristics of the groundwater aquifers east of Wadi El-Natron, Egypt. *NRIAG Journal of Astronomy and Geophysics*, **5**, 1, 124–146, doi: 10.1016/j.nrjag.2015.12.001.
- Salem Z. E., Osman M. O., 2017: Use of major ions to evaluate the hydrogeochemistry of groundwater influenced by reclamation and seawater intrusion, West Nile Delta, Egypt. *Environ. Sci. Pollut. Res.*, **24**, 4, 3675–3704, doi: 10.1007/s11356-016-8056-4.
- Salheen M. A., 2013: Towards a water based regional development model for Siwa Oasis in the Western Desert of Egypt. In: *Proceedings of AASTMT Conference 2013: Global Climate Change. Biodiversity and Sustainability*, April 2013, Cairo, available at <http://projects.upei.ca/climate/files/2012/07/Global-Climate-Change-Biodiversity-and-Sustainability-2015.pdf>.
- Schneidhofer P., Nau E., Hinterleitner A., Lugmayr A., Bill J., Gansum T., Paasche K., Seren S., Neubauer W., Draganits E., Trinks I., 2017: Palaeoenvironmental analysis of large-scale, high-resolution GPR and magnetometry data sets: the Viking Age site of Gokstad in Norway. *Archaeol. Anthropol. Sci.*, **9**, 6, 1187–1213, doi: 10.1007/s12520-015-0312-x.
- Semerjian L. A., 2011: Quality assessment of various bottled waters marketed in Lebanon. *Environ. Monit. Assess.*, **172**, 1-4, 275–285, doi: 10.1007/s10661-010-1333-7.

- Shebl A., Abdellatif M., Elkhateeb S. O., Csámer Á., 2021: Multisource data analysis for gold potentiality mapping of Atalla area and its environs, Central Eastern Desert, Egypt. *Minerals*, **11**, 6, 641, doi: 10.3390/min11060641.
- Subba Rao N., 2006: Seasonal variation of groundwater quality in a part of Guntur District, Andhra Pradesh, India. *Environ. Geol.*, **49**, 3, 413–429, doi: 10.1007/s00254-005-0089-9.
- Todd D. K., 1980: *Groundwater Hydrology*. 2nd ed., John Wiley and Sons, Inc, New York, 535 p.
- Vega M., Pardo R., Barrado E., Debán L., 1998: Assessment of seasonal and polluting effects on the quality of river water by exploratory data analysis. *Water Res.*, **32**, 12, 3581–3592, doi: 10.1016/S0043-1354(98)00138-9.
- Wang S., Zheng W., Currell M., Yang Y., Zhao H., Lv M., 2017: Relationship between land-use and sources and fate of nitrate in groundwater in a typical recharge area of the North China Plain. *Sci. Total Environ.*, **609**, 607–620, doi: 10.1016/j.scitotenv.2017.07.176.
- Xiao J., Jin Z. D., Zhang F., Wang J., 2012: Solute geochemistry and its sources of the groundwater in the Qinghai Lake catchment, NW China. *J. Asian Earth Sci.*, **52**, 21–30, doi: 10.1016/J.JSEAES.2012.02.006.
- Yousef A. F., 2010: Impact of human activities on groundwater depletion and quality deterioration in the northwestern shelf of Nubian sandstone and fractured carbonate aquifer systems. Sustainable development in dry lands—meeting the challenge of global climate change. *Proceedings of the Ninth International Conference on Development of Dry lands*, Alexandria, Egypt. 411–427.